Marine Energy Research

SCIEPublish

Article

Hydrodynamic Performance and Wave Attenuation Mechanism of a Single-Ring Floating Breakwater with Internal Compartmentalization and Ballasted Water

Jijian Lian [1,2], Yicheng Liu [1,2], Xiuwei Yang [1,2,*], Ye Yao [1,2], Shiqi Wang [1,2] and Jianchao Wang [1,2]

[1] School of Ocean Energy, Tianjin University of Technology, Tianjin 300384, China; jjlian@tju.edu.cn (J.L.); cheng03152021@163.com (Y.L.); yaoye-111@163.com (Y.Y.); 20010126@stud.tjut.edu.cn (S.W.); 18830237959@163.com (J.W.)

[2] Tianjin Key Laboratory of Marine Clean Energy Development and Utilization, Tianjin University of Technology, Tianjin 300384, China

* Corresponding author. E-mail: yangxw@email.tjut.edu.cn (X.Y.)

Received: 20 August 2026; Revised: 7 September 2026; Accepted: 9 September 2026; Available online: 23 September 2026

ABSTRACT: A three-dimensional, two-way coupled fluid–structure interaction (FSI) numerical model was established to investigate the hydrodynamic performance and wave-attenuation mechanism of a water-ballasted single-ring floating breakwater with internal compartmentalization. The model couples the CFD wave solver in OpenFOAM with its built-in six-degree-of-freedom rigid-body motion solver and the dynamic mooring solver MoorDyn. It was validated against two benchmark cases comprising physical wave-flume measurements and published numerical results. Four configurations—unballasted, single-compartment, dual-compartment, and four-compartment—were compared under extreme irregular waves, with different incident-wave headings considered for the compartmentalized configurations. The analysis focused on wave transmission, transient mooring tension, and the combined effects of annular wave scattering and ballast-water sloshing. The results demonstrate that the four-compartment configuration provides the strongest wave attenuation, whereas the dual-compartment configuration achieves a better balance between wave-attenuation performance and mooring-load distribution.

Keywords: Floating breakwater; Water ballast; Tuned liquid damper (TLD); Fluid-structure interaction (FSI); Compartmentalization; Mooring tension

1. Introduction

Breakwaters play a critical role in protecting coastal and offshore facilities by reducing incident-wave energy and creating sheltered waters. This protective function is becoming increasingly important as floating infrastructure is increasingly deployed in exposed marine environments. Among emerging offshore applications, floating photovoltaic (FPV) systems have attracted considerable attention due to their water-cooling benefits and distinctive hydroelastic characteristics [1,2]. Previous studies have investigated their power-generation performance, structural design, experimental evaluation, and panel-cooling mechanisms

© 2026 The authors. This is an open access article under the Creative Commons Attribution 4.0 International License (https://creativecommons.org/licenses/by/4.0/).

[3–6], while their substantial deployment potential in reservoirs and open marine environments has further stimulated interest in offshore applications [7–9]. However, compared with installations in sheltered inland waters, offshore floating facilities are exposed to more severe hydrodynamic conditions, under which wave-induced forces and impulsive loads may threaten structural integrity, operational stability, and long-term serviceability [10–12]. Floating breakwaters (FBWs) provide a flexible means of protecting such facilities, particularly where the construction of fixed breakwaters is constrained by large water depths, unfavorable seabed conditions, or environmental requirements [13–15]. Their modular construction, reloadability, and limited disturbance to the seabed make them particularly attractive for deep-water and environmentally sensitive sites.

The structural forms of FBWs have progressively evolved from conventional pontoons toward geometrically modified, porous, and water-ballasted configurations [16]. Conventional pontoon- and box-type FBWs attenuate waves mainly through reflection and are generally more effective when the incident wavelength is short relative to the characteristic width of the structure [17,18]. Their attenuation performance can deteriorate substantially under long-period waves, particularly when large rigid-body motions increase wave transmission and mooring demand. To overcome this limitation, researchers have proposed dual-pontoon configurations [19] and geometric, winged, or porous modifications designed to enhance wave reflection and promote vortex-induced energy dissipation [20–22]. Tuned liquid damper principles have also provided a new basis for controlling the dynamic responses of floating structures through internal liquid motion [23,24]. Water-ballasted FBWs utilize internal sloshing and viscous dissipation to convert and dissipate part of the incident-wave energy [25], while subsequent studies have investigated the effects of structural shape, ballast-water depth, and internal baffles on wave attenuation and sloshing suppression [26,27]. Nevertheless, existing studies have primarily focused on rectilinear box- or I-shaped structures, individual ballast parameters, and regular-wave conditions. Systematic comparisons among unballasted, single-, dual-, and four-compartment layouts within a closed annular structure remain limited. Moreover, the heading-dependent three-dimensional interactions among external waves, internal sloshing, rigid-body motion, and dynamic mooring loads have not been adequately clarified.

The hydrodynamic performance of FBWs has been investigated using analytical theory, physical model testing, and numerical simulation [18–29]. Potential-flow and semi-analytical methods can efficiently predict wave diffraction, radiation, reflection, and transmission under small-amplitude wave assumptions. However, they cannot directly resolve viscous energy dissipation, turbulence, vortex shedding, flow separation, or violent internal sloshing. Physical experiments provide direct measurements of wave transmission, structural motion, and mooring forces, but facility dimensions, instrumentation, and experimental costs often constrain the range of parameters investigated and the observation of internal flow fields. Computational fluid dynamics and related high-fidelity numerical methods are better suited to resolving nonlinear free-surface deformation, transient flow separation, and viscous energy dissipation [30,31], although they require substantially greater computational resources.

Fluid–structure coupling strategies can be broadly classified into hydroelastic and rigid-body approaches. Hydroelastic models simultaneously resolve hydrodynamic loading and structural stress–deformation responses and are required when structural flexibility materially influences hydrodynamic behavior. Rigid-body coupling, by contrast, neglects structural deformation and determines the six-degree-of-freedom motion of the structure under external hydrodynamic loads. Tightly coupled CFD–six-degree-of-freedom solvers provide an effective framework for predicting the global motions of floating offshore structures [32]. Incorporating dynamic mooring models further enables the interactions among waves, floating bodies, and restraining lines to be resolved [33–36]. Related CFD–multibody-dynamics, hydroelastic–mooring, and OpenFOAM-based mooring-coupling studies have demonstrated that structural flexibility, mooring stiffness, and dynamic damping can significantly influence the predicted hydrodynamic response [37–40]. Because the present study focuses on global structural motion, ballast-water sloshing, wave

transmission, and mooring response rather than local structural stress and deformation, the floating breakwater is treated as a rigid body. A fully coupled fluid–structure interaction (FSI) framework is therefore established in OpenFOAM by integrating the six-degree-of-freedom motion solver with MoorDyn [41–45].

Existing coupled numerical methods provide the capability to simulate wave–body–mooring interactions, but the attenuation physics of internally compartmentalized, water-ballasted annular FBWs remains insufficiently understood. In particular, the closed annular geometry produces three-dimensional scattering and direction-dependent internal flow paths that differ fundamentally from those of conventional rectilinear ballast tanks. The combined influences of compartment number and incident-wave heading on wave transmission and mooring-load redistribution under extreme irregular waves remain unresolved. Accordingly, this study establishes a three-dimensional, fully coupled fluid–structure interaction (FSI) framework that incorporates the mooring system to investigate these effects in a water-ballasted single-ring FBW.

The remainder of this paper is organized as follows. Section 2 presents the governing equations and the OpenFOAM–MoorDyn coupling procedure. Section 3 validates the established model against physical experimental measurements and published numerical results. Section 4 describes the computational setup and examines the overall wave field and attenuation mechanisms. Section 5 compares the wave-transmission and mooring-tension responses of the four compartmentalization configurations. Section 6 summarizes the principal conclusions and limitations.

2. Numerical Model

2.1. Governing Equations

2.1.1. Fluid Governing Equations

The flow field is simulated using waveFoam within the OpenFOAM framework. Wave generation and absorption are implemented using the relaxation-zone approach described by Jacobsen et al. [46]. The incompressible Reynolds-averaged Navier–Stokes equations are discretized using the finite-volume method, and the air–water interface is captured using the volume-of-fluid method originally proposed by Hirt and Nichols [47]. Equations (1)–(4) follow the standard two-phase incompressible flow formulation adopted in OpenFOAM [47,48]. The continuity equation is expressed as:

$$\nabla \cdot \mathbf{U} = 0 \tag{1}$$

where ∇ is the spatial differential operator and $\mathbf{U}$ is the fluid-velocity vector.

The momentum equation is written as:

$$\frac{\partial(\rho \mathbf{U})}{\partial t} + \nabla \cdot (\rho \mathbf{U}\mathbf{U}) = -\nabla p_d + \nabla \cdot \left[\mu_{\text{eff}}(\nabla \mathbf{U} + (\nabla \mathbf{U})^T)\right] - (\mathbf{g} \cdot \mathbf{x})\nabla \rho + \mathbf{f}_\sigma \tag{2}$$

where ρ is the local mixture density; t is time; $\mathbf{U}\mathbf{U}$ is the dyadic product of the velocity vector and is therefore a second-order tensor; p_d is the modified dynamic pressure with the hydrostatic contribution removed; μ_{eff} is the equivalent dynamic viscosity; $\mathbf{g}$ is the gravitational-acceleration vector; $\mathbf{x}$ is the position vector; and $\mathbf{f}_\sigma$ is the volumetric surface-tension force vector.

Following the compressive VOF formulation implemented in OpenFOAM [47,48], an artificial interface-compression term is introduced into the conventional volume-fraction transport equation to reduce numerical diffusion and maintain a sharp air–water interface:

$$\frac{\partial \alpha}{\partial t} + \nabla \cdot (\alpha \mathbf{U}) + \nabla \cdot [\alpha(1-\alpha)\mathbf{U}_r] = 0 \tag{3}$$

where α represents the water phase volume fraction ($\alpha = 1$ in water, $\alpha = 0$ in air). $\mathbf{U}_r$ is the relative compression velocity. The fluid density ρ is calculated via a weighted average based on the volume fraction:

$$\rho = \alpha \rho_{water} + (1 - \alpha) \rho_{air} \tag{4}$$

2.1.2. Structural Governing Equations

The six-degree-of-freedom motion response of the floating structure is calculated using OpenFOAM's built-in sixDoFRigidBodyMotion solver. Following the tightly coupled CFD–6DOF formulation described by Dunbar et al. [32], the translational and rotational motions of the rigid body are governed by the Newton–Euler equations, which express conservation of linear and angular momentum, respectively:

$$m_i \ddot{\mathbf{x}}_i = \mathbf{F}_i \tag{5}$$

$$\mathbf{I}_i \dot{\boldsymbol{\omega}}_i + \boldsymbol{\omega}_i \times (\mathbf{I}_i \boldsymbol{\omega}_i) = \mathbf{M}_i \tag{6}$$

where the subscript i denotes the index of the floating body. m_i and $\mathbf{I}_i$ represent the mass and moment of inertia matrix of the floating body, respectively; $\ddot{\mathbf{x}}_i$ and $\dot{\boldsymbol{\omega}}_i$ are the linear and angular accelerations of the body's center of mass. The total external force $\mathbf{F}_i$ and total moment $\mathbf{M}_i$ acting on the floating body can be decomposed as follows:

$$\mathbf{F}_i = \int_S (-p\mathbf{I} + \boldsymbol{\tau}) \cdot \mathbf{n} \, d\mathbf{S} + \mathbf{F}_{mooring} + m_i \mathbf{g} \tag{7}$$

$$\mathbf{M}_i = \int_S \mathbf{r} \times (-p\mathbf{I} + \boldsymbol{\tau}) \cdot \mathbf{n} \, d\mathbf{S} + \mathbf{r}_{mooring} \times \mathbf{F}_{mooring} \tag{8}$$

where the first term on the right side of the equations represents the hydrodynamic load, obtained by integrating the normal pressure p and tangential viscous shear stress $\boldsymbol{\tau}$ over the wetted surface $\mathbf{S}$ of the floating body ($\mathbf{I}$ is the identity matrix, $\mathbf{n}$ is the surface normal vector). $\mathbf{F}_{mooring}$ is the nonlinear restoring force of the mooring system; $\mathbf{r}$ and $\mathbf{r}_{mooring}$ are the moment arm vectors of the hydrodynamic and mooring forces relative to the center of mass, respectively. Assuming the center of mass coincides with the center of rotation, these lever arms define the rotational torque.

2.1.3. Mooring Line Governing Equations

The nonlinear dynamic response of the mooring system is simulated using MoorDyn [41,43]. Following its lumped-mass formulation [41], each continuous mooring line is discretized into a series of elastic line segments connected by nodes, with half the mass of each adjacent segment assigned to the shared node. The transient motion equation for any node i is:

$$(m_i + a_i)\ddot{\mathbf{r}}_i = \mathbf{T}_i - \mathbf{T}_{i-1} + \mathbf{C}_i - \mathbf{C}_{i-1} + \mathbf{W}_i + \mathbf{B}_i + \mathbf{F}_{dp,i} + \mathbf{F}_{dt,i} \tag{9}$$

where m_i and a_i are the lumped mass and hydrodynamic added mass of the node i; $\ddot{\mathbf{r}}_i$ is the node acceleration. $\mathbf{T}$ and $\mathbf{C}$ are the axial tension and internal damping forces of adjacent segments,

respectively; $\mathbf{W}_i$ and $\mathbf{B}_i$ are the buoyant weight of the node and the vertical reaction force of the seabed, respectively; $\mathbf{F}_{dp,i}$ and $\mathbf{F}_{dt,i}$ are the normal and tangential fluid drag components acting on the node.

The mooring line segments between adjacent nodes are treated as elastic units subjected solely to axial tension [41]. When the segment's instantaneous length L exceeds its unstressed initial length L_0, the axial tension is given by Hooke's law:

$$T_j = \frac{EA}{L_{0,j}}(Lj - L_{0,j}) \tag{10}$$

where T_j is the scalar axial-tension magnitude; E is the elastic modulus of the material, A is the cross-sectional area; T_j is the instantaneous length of the segment j; $L_{0,j}$ is its unstretched length, and $\frac{EA}{L_{0,j}}$ represents the axial stiffness of the mooring segment. When $L_j \leq L_{0,j}$, assuming the cable possesses no compressive resistance, the tension $T_j = 0$. The internal damping force accounts for energy dissipation during dynamic stretching, which is proportional to the segment's strain rate.

2.2. Coupling Algorithm

The mooring system is two-way coupled with OpenFOAM through a dedicated coupling interface. At each coupling time step, OpenFOAM passes the displacement and velocity of the floating body to MoorDyn. MoorDyn then calculates the instantaneous mooring forces and moments and returns them to the rigid-body motion solver, where they are incorporated as external loads into the 6DOF equations of motion. This process iterates within the time step, enabling the fully coordinated resolution of the fluid, structure, and mooring systems (the coupling workflow is shown in Figure 1).

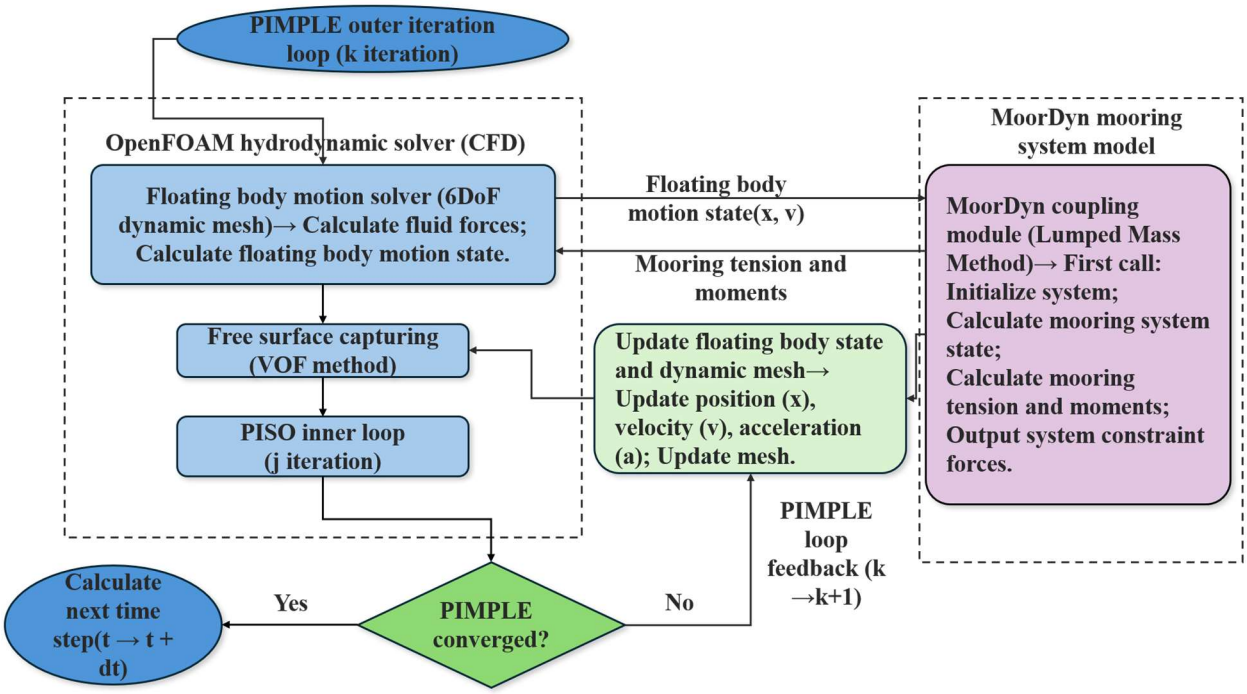


Figure 1. Flowchart of the OpenFOAM-MoorDyn coupling procedure.

During the numerical solution, pressure–velocity coupling is handled using the PIMPLE algorithm, which combines SIMPLE-type outer iterations with PISO-type pressure-correction loops. This approach

improves convergence and numerical stability when relatively large time steps are employed, making it suitable for transient fluid–structure interaction simulations involving substantial mesh deformation.

The temporal and spatial terms in the governing equations are discretized as follows. The temporal derivative terms are discretized using a second-order implicit scheme, while the gradient terms are evaluated using the Gauss linear scheme. Different discretization schemes are adopted for the convective terms: the convective term in the momentum equation is discretized using the Gauss vanLeer second-order TVD scheme, whereas that in the phase-fraction transport equation is discretized using the Gauss vanLeer second-order TVD scheme. The Laplacian terms are discretized using the Gauss linear corrected scheme to account for mesh non-orthogonality. Linear interpolation is applied to all field variables, and surface-normal gradients are evaluated using a corrected scheme to reduce errors associated with mesh non-orthogonality.

To accommodate the large-amplitude motion of the floating body, a dynamic mesh method is employed at the fluid–structure interface. The computational domain is divided into a fixed mesh region and a body-fitted deforming mesh region. As the floating body undergoes translational and rotational motions, the coordinates of the mesh nodes in the deforming region are updated at each time step according to the body motion, allowing the mesh to deform smoothly while the fixed mesh region remains unchanged. This procedure maintains mesh conformity between the fluid domain and the moving solid boundary throughout the simulation.

3. Model Validation

To assess the accuracy and reliability of the three-dimensional fully coupled nonlinear numerical model developed in this study, two complementary validation studies were conducted using physical wave-tank experimental data and published numerical benchmark results.

3.1. Validation Against Physical Experiments

The physical model tests conducted by Yuan et al. (2025) [45] are adopted as the first benchmark validation case. The tests were performed in a wave flume using a 1:60-scale rectangular water-ballasted floating-breakwater model restrained by four catenary mooring lines. The geometry, principal dimensions, and mooring arrangement of the physical model are illustrated in Figure 2. Regular waves with incident heights ranging from 0.08 to 0.30 m and periods ranging from 1.0 to 2.0 s were generated to investigate wave transmission, pitch motion, and mooring-tension response. The validation results presented in Figure 3 correspond specifically to a regular-wave condition with an incident wave height of 0.08 m and a wave period of 1.5 s at model scale. The present numerical domain reproduces the principal model geometry, water depth, mooring arrangement, wave-gauge locations, and validation wave condition adopted in the physical experiments.

Based on the experimental setup shown in Figure 2, Figure 3 compares the key transient response time histories obtained from numerical simulations and physical experiments under the regular-wave condition of $H = 0.08m$ and $T = 1.5s$ at the model scale. The quantities examined include the weather-side and lee-side wave elevations, the transient response of the primary load-bearing mooring line on the weather side, and the pitch response of the breakwater. All subplots are presented over the same steady-state time interval to facilitate direct comparison. No temporal stretching or amplitude scaling was applied to either dataset.

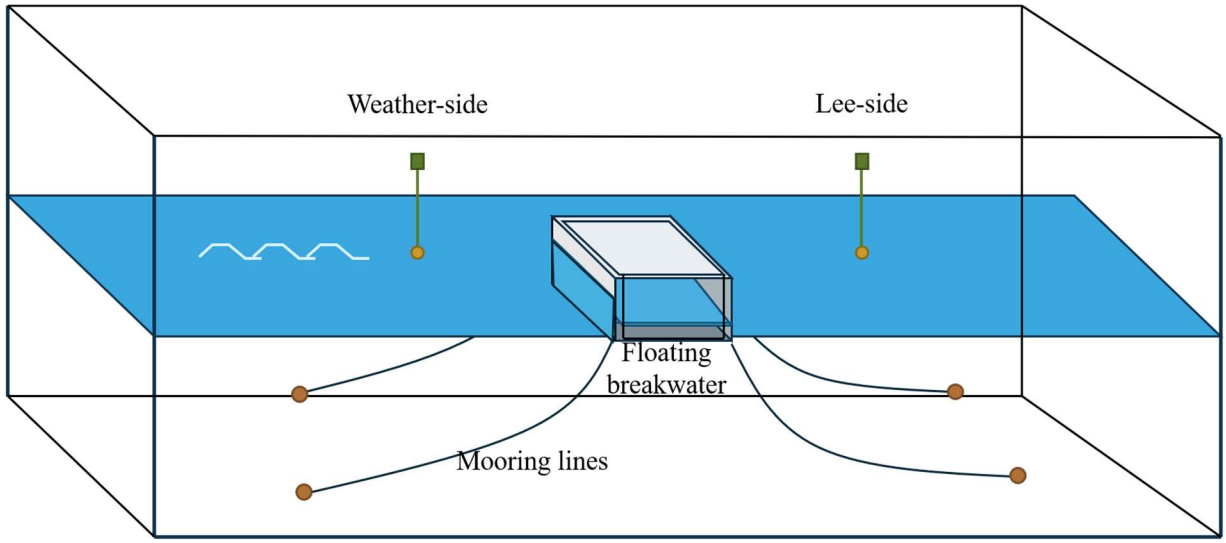


Figure 2. Schematic of the experimental wave-flume setup, water-ballasted floating-breakwater model, wave-gauge arrangement, and catenary mooring lines system.

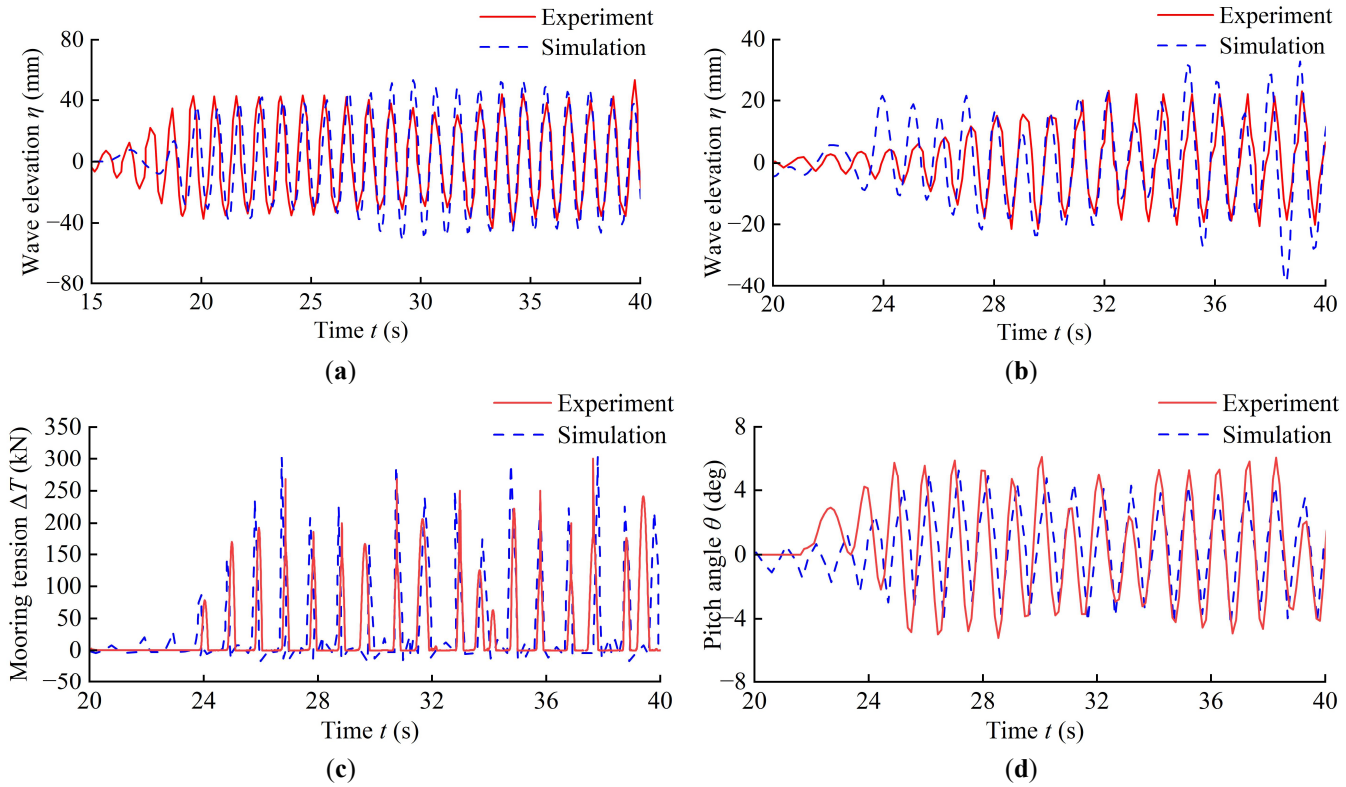


Figure 3. Comparison of numerical and experimental transient responses under the regular-wave condition of $H = 0.08m$ and $T = 1.5s$. (**a**) Weather-side wave elevation; (**b**) Lee-side wave elevation; (**c**) Weather-side mooring tension; (**d**) Pitch motion response.

In Figure 3c, the plotted mooring quantity is the dynamic axial-tension increment, defined as $\Delta T = T_{(t)} - T_0$, where T_0 is the still-water pretension. Accordingly, positive values indicate an increase above the initial pretension, whereas the small negative values indicate that the instantaneous tension temporarily falls below T_0. They do not represent compressive loading in the mooring line, because the line is modeled as a tension-only element.

The comparative results show that the numerical predictions obtained using the present OpenFOAM model agree well with the physical experimental measurements in terms of both phase evolution and peak-to-trough response amplitudes. In particular, the model demonstrates good fidelity in reproducing pronounced nonlinear features, including crest–trough asymmetry and transient high-frequency fluctuations in mooring tension. These comparisons support the reliability of the adopted fluid–structure interaction algorithm and mesh discretization strategy for simulating complex wave–body interactions.

3.2. Validation Against Published Numerical Results

In addition to validation against the physical experiments, the present computational results are further compared with those obtained using an independent numerical model developed by Lian et al. (2026) [49]. This second benchmark case is used to assess the numerical stability and reliability of the present model under extreme wave-steepness conditions. As illustrated in Figure 4, the benchmark configuration consists of an annular floating breakwater deployed in a rectangular numerical wave tank and restrained by a symmetric four-point mooring system. Two wave gauges are positioned on the weather side and lee side of the breakwater to record the corresponding free-surface elevations. To ensure a consistent basis for comparison, the present model reproduces the principal structural geometry, water depth, mooring arrangement, wave-gauge locations, and incident-wave conditions adopted in the reference numerical model.

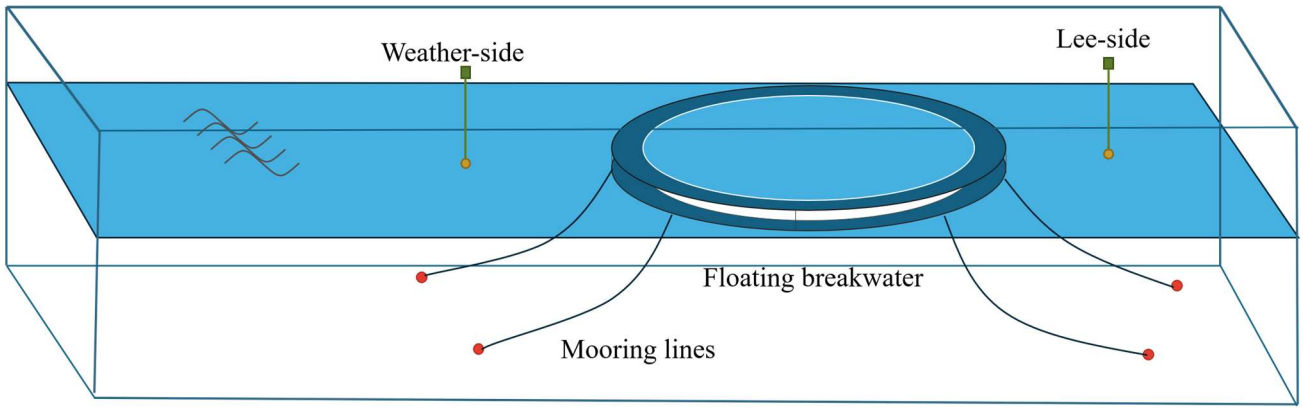
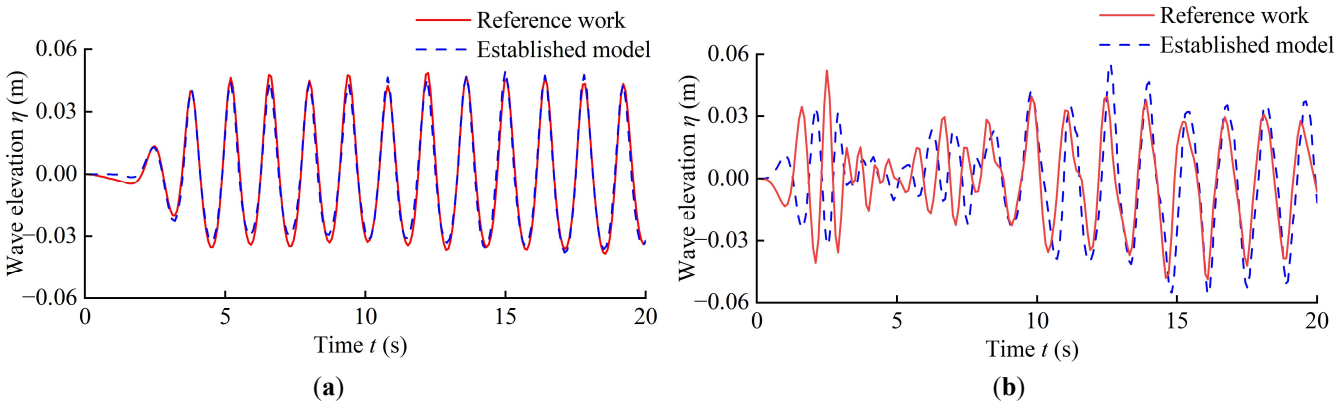


Figure 4. Schematic of the numerical wave tank, floating-breakwater configuration, and mooring lines arrangement for the cross-validation case.

Based on the benchmark configuration shown in Figure 4, Figure 5 presents detailed comparisons between the present fully coupled model and the reference numerical model. The quantities examined include the time histories of the weather-side and lee-side wave elevations, the tension in the primary load-bearing mooring line on the weather side, and the pitch response of the floating breakwater.



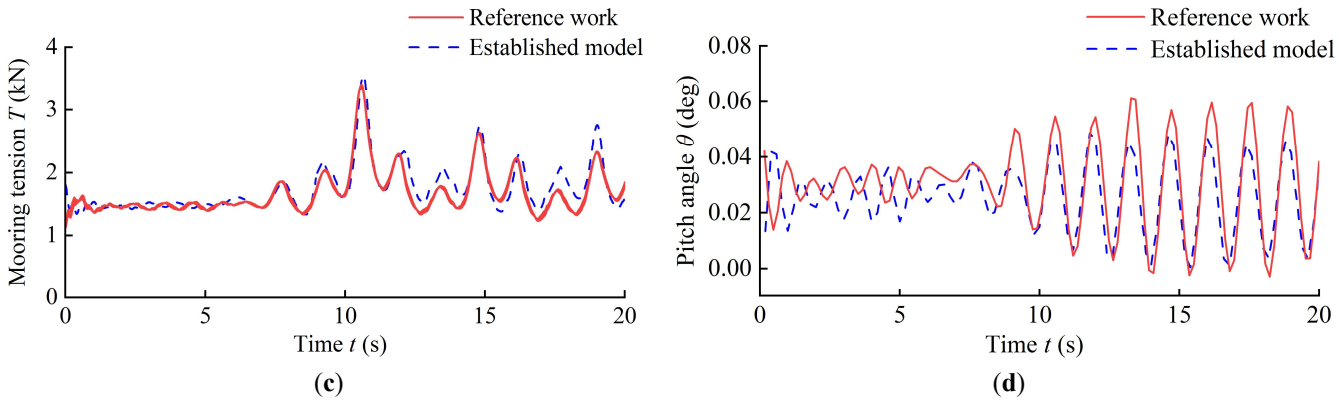


Figure 5. Cross-validation results between the present coupled model and the reference numerical model. (**a**) Weather-side wave elevation; (**b**) Lee-side wave elevation; (**c**) Weather-side mooring tension; (**d**) Pitch motion response.

To quantify the level of agreement, the peak-to-peak amplitude $Q_{pp} = Q_{\max} - Q_{\min}$ is calculated over the steady-state comparison interval for each response quantity. The corresponding amplitude agreement is defined as $A_Q = [1 - |Q_{pp,present} - Q_{pp,ref}|/Q_{pp,ref}] \times 100\%$. This percentage measures agreement in response amplitude and should not be interpreted as point-by-point agreement between the two time histories; phase consistency is assessed separately from the temporal evolution of the curves.

The comparisons show that the present fully coupled model reproduces the principal response frequencies, phase evolution, and amplitude envelopes obtained from the reference numerical model. Based on the peak-to-peak amplitudes, the agreement percentages for the weather-side wave elevation, lee-side wave elevation, weather-side mooring tension, and pitch response are 6.5%, 9.6%, 12%, and 12.5%, respectively. The remaining differences are most evident in the lee-side free-surface fluctuations and pitch-response envelope. These differences are attributable to the different hydrodynamic formulations: the present model resolves viscous dissipation, nonlinear free-surface deformation, and dynamically coupled mooring loads, whereas the reference model employs different assumptions and numerical treatments. Therefore, the comparison demonstrates consistency in the overall response characteristics rather than exact pointwise equivalence.

4. Wave Attenuation Performance and Analysis of Hydrodynamic Characteristics

4.1. Model Setup

This study focuses on a single-ring floating breakwater with various internal compartmentalization configurations. The main structure is modeled as a hollow annular floating body. To maintain dynamic similarity between the model and prototype, the geometric and inertial properties are scaled according to the Froude similarity criterion at a geometric scale of 1:50. As illustrated in Figure 6, the model-scale structure has an inner diameter of 2.64 m, an outer diameter of 2.96 m, an overall height of 0.10 m, and a uniform wall thickness of 0.01 m. The prescribed dry rigid-body mass is 32.94 kg, with a center of gravity at (0.0, 0.0, −0.007) m and principal moments of inertia of (32.50, 32.50, 64.93) kg·m^2. The same dry-structure mass properties are prescribed for all four configurations. For the 1C-B, 2C-B, and 4C-B configurations, an initial ballast-water depth of 0.057 m is specified within the annular cavity. Based on the effective internal diameters of 2.94 and 2.66 m, this filling depth corresponds to a ballast-water volume of 0.07020 m^3 and a ballast-water mass of 70.20 kg, giving a total physical mass of 103.14 kg for each ballasted configuration. Neglecting the vertical component of the mooring pretension and the volume occupied by the internal baffles, the corresponding theoretical unmoored equilibrium drafts are 0.0234 m for the Empty configuration and 0.0733 m for the ballasted configurations. A Cartesian coordinate system is defined with its origin at the geometric center of the structure on the still-water surface. The positive x-

axis is aligned with the wave-propagation direction, while the positive *z*-axis points vertically upward, as also shown in Figure 6. The sheltered floating photovoltaic (FPV) facility is represented by an equivalent rigid body with a model-scale mass of 32.94 kg. The detailed dynamic properties of the floating structure, including its equivalent mass, center of gravity, and moments of inertia, together with the physical properties of the mooring lines, are summarized in Table 1.

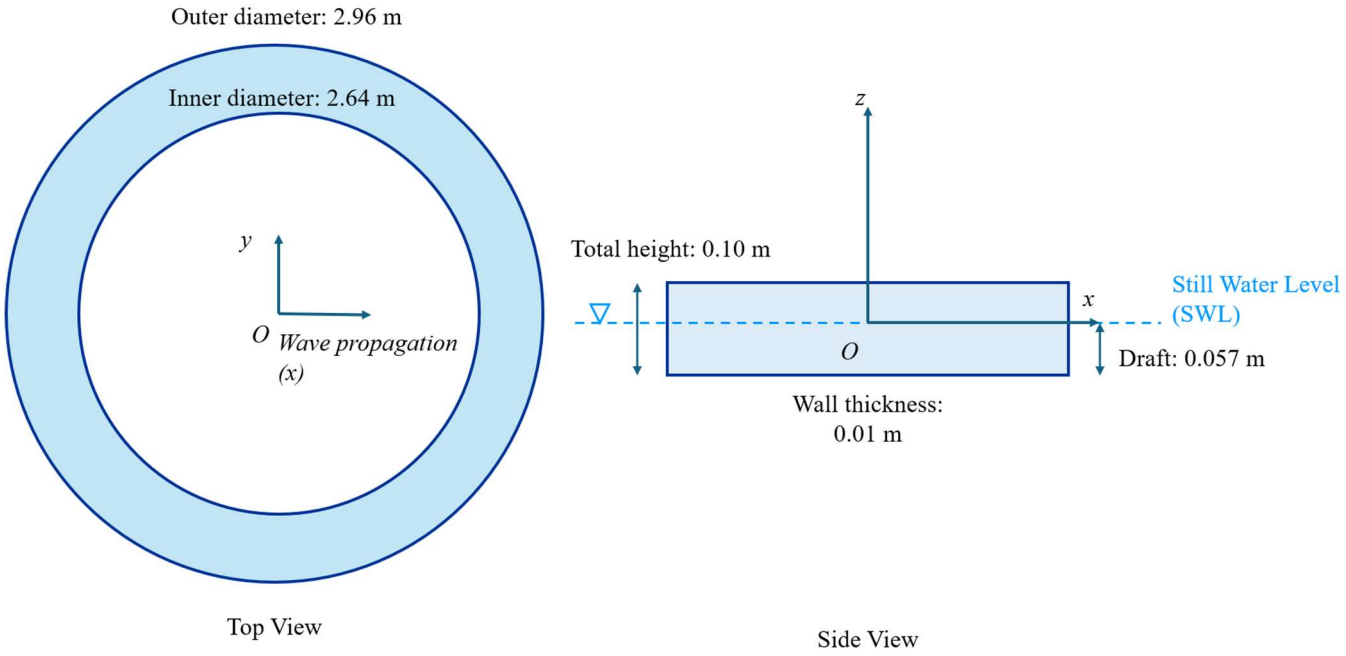


Figure 6. Schematic diagram of the geometric dimensions and coordinate system of the single-ring floating breakwater.

Table 1. Parameters of the FPV structure and mooring lines.

Category	Parameter	Value
Floating structure	Mass	32.94 kg
	Centre of mass (COG)	(0.0, 0.0, −0.007) m
	Moment of inertia	(32.5, 32.5, 64.93) kg·m^2
Mooring system	Number of mooring lines	12
	Mooring layout	Four anchors and twelve chains
	Chain diameter	0.002 m
	Mass per unit length	0.0630 kg·m^{-1}
	Axial stiffness (EA)	259 N
	Drag coefficient (C_d)	1.6
	Added mass coefficient (C_a)	1.0

To ensure adequate station-keeping performance under complex wave conditions, a three-dimensional symmetric mooring system comprising four seabed anchors and twelve anchor chains is employed, as illustrated in Figure 7. Twelve circular fairleads are uniformly distributed along the bottom circumference of the floating structure as mooring connection points. At the model scale, the unstretched length of each anchor chain is set to either 1.2 or 1.9 m, depending on the distance between the corresponding seabed anchor and structural fairlead. In MoorDyn, the mooring lines are represented as geometrically nonlinear, tension-only, axially elastic elements, with an axial stiffness EA of 259 N at model scale. Therefore, dynamic axial elongation, internal damping, hydrodynamic drag, added mass, and seabed contact are included in the severe-wave simulations. However, bending and torsional stiffness, plastic deformation, chain-link failure, anchor failure, and nonlinear seabed-soil interaction are not considered. The three-

dimensional coordinates of the seabed anchors and fairleads, together with the connectivity and unstretched length of each mooring line, are summarized in Table 2.

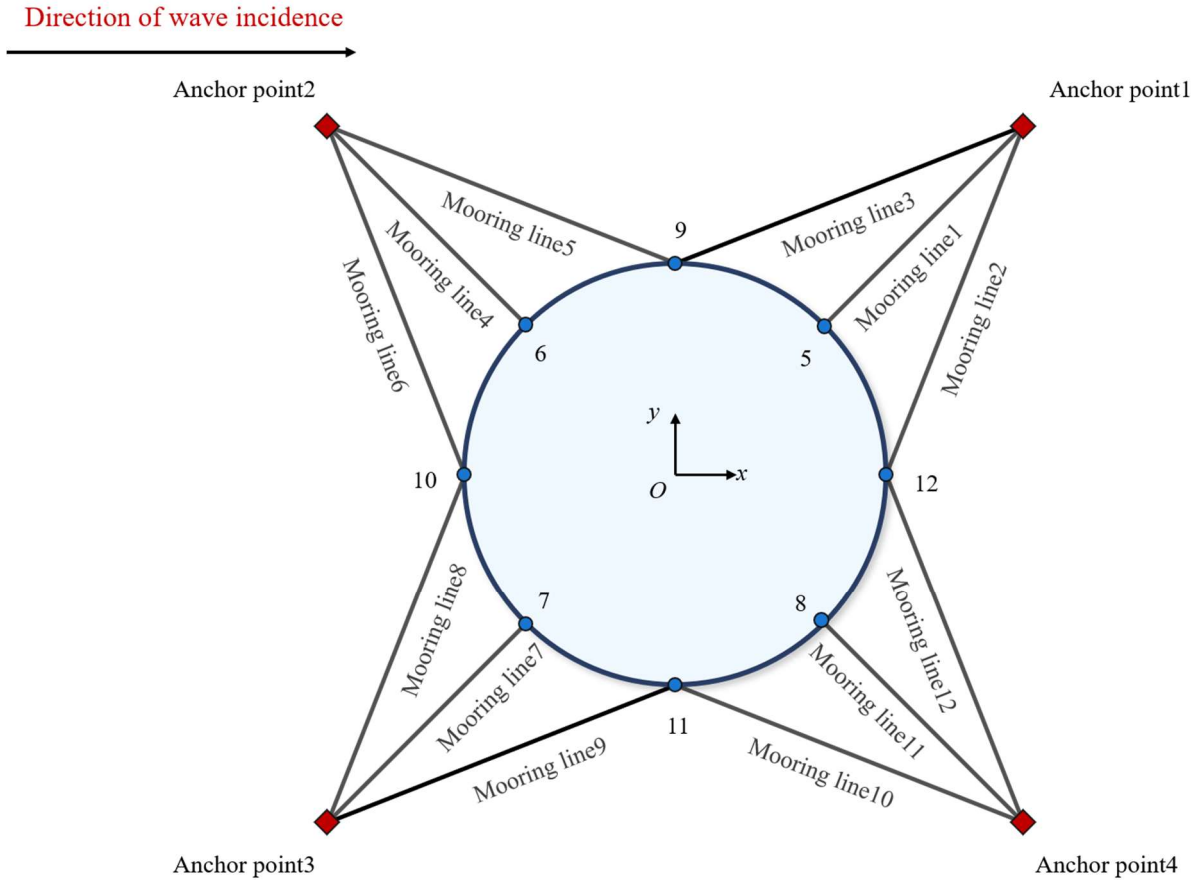


Figure 7. Layout diagram of the 3D symmetrical mooring system.

Table 2. Configuration and coordinates of the mooring system used in the numerical model.

ID	Type	X (m)	Y (m)	Z (m)	Anchor ID	Fairlead ID	Unstretched Length (m)
1	Anchor	1.8602	1.8602	−0.34	1	5	1.2
2	Anchor	−1.8602	1.8602	−0.34	1	9	1.9
3	Anchor	−1.8602	−1.8602	−0.34	1	10	1.9
4	Anchor	1.8602	−1.8602	−0.34	2	6	1.2
5	Fairlead	1.0465	1.0465	−0.057	2	10	1.9
6	Fairlead	−1.0465	1.0465	−0.057	2	11	1.9
7	Fairlead	−1.0465	−1.0465	−0.057	3	7	1.2
8	Fairlead	1.0465	−1.0465	−0.057	3	11	1.9
9	Fairlead	1.48	0	−0.057	3	12	1.9
10	Fairlead	0	1.48	−0.057	4	8	1.2
11	Fairlead	−1.48	0	−0.057	4	12	1.9
12	Fairlead	0	−1.48	−0.057	4	9	1.9

To improve computational efficiency and numerical robustness, all simulations are conducted at the model scale. The geometric dimensions, mass properties, and load-related parameters are scaled according to the Froude similarity criterion at a geometric scale of 1:50. The numerical results are subsequently converted to prototype-scale values for analysis. As illustrated in Figure 8, the three-dimensional numerical wave tank has dimensions of 21 m × 6 m × 1 m in the length, width, and height directions, respectively. To adequately resolve flow separation around the breakwater and the associated wave–structure interactions,

local mesh refinement is applied near the fluid–structure interface and in regions with pronounced free-surface variation. A nonuniform graded mesh is employed elsewhere to achieve an appropriate balance between numerical accuracy and computational efficiency.

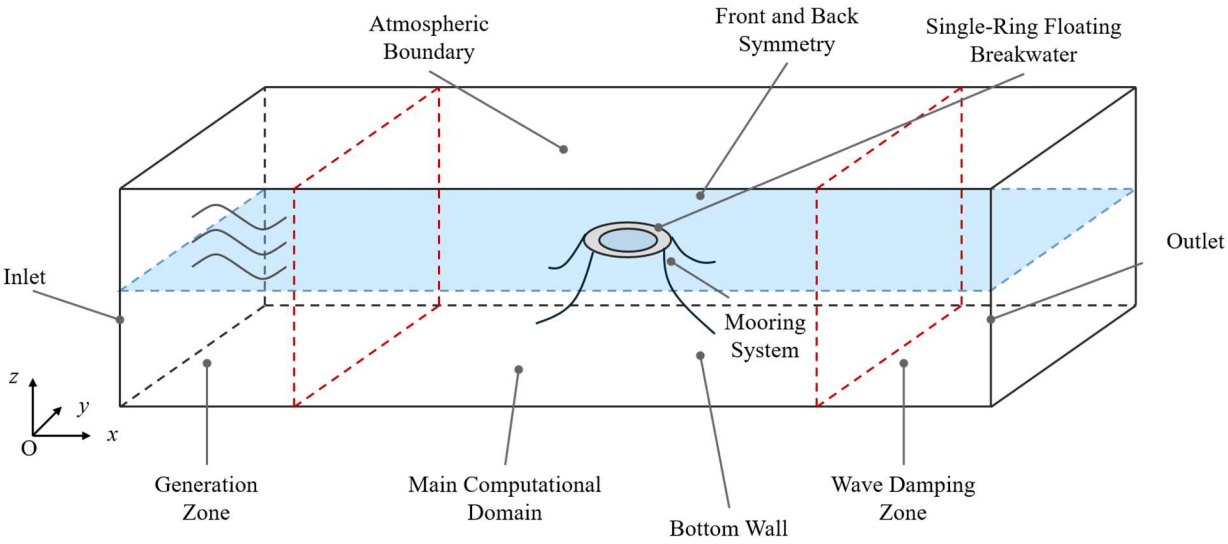


Figure 8. Setup of the 3D computational domain and boundary conditions for the numerical wave tank.

Based on the established numerical wave tank and grid layout described above, accurate wave generation is essential for the subsequent hydrodynamic analysis. To simulate the dynamic responses of the floating breakwater under realistic ocean conditions, irregular waves are generated in the numerical wave tank based on the JONSWAP spectrum. The irregular wave elevation is synthesized by the linear superposition of $N = 200$ discrete regular wave components using the random phase method. According to the OpenFOAM waveProperties configuration, the peak enhancement factor (γ) is set to 3.3. For the extreme sea state investigated in this study, the significant wave height (H_s) and peak period (T_p) at model scale (1:50) are specified as 0.12 m and 1.4 s, respectively. Furthermore, spatial relaxation zones are implemented at both the inlet and outlet boundaries to prevent unphysical wave reflections. The detailed parameters for the irregular wave generation are summarized in Table 3.

Table 3. Parameters of the incident irregular wave in the numerical model (1:50 scale).

Parameter	Symbol	Value	Unit
Wave spectrum type	-	JONSWAP	-
Water depth	d	0.34	m
Significant wave height	H_s	0.08/0.12	m
Peak period	T_p	1.4	s
Peak enhancement factor	-	3.3	-
Number of wave components	γ	200	-
Wave propagation direction	-	0	°
Phase distribution method	-	Random phase	-

4.2. Mesh-Independent Study

To assess the influence of spatial discretization on the fluid–structure interaction results, structured hexahedral meshes were adopted throughout the computational domain, and three mesh-resolution levels—coarse, medium, and fine—were constructed. Mesh convergence was evaluated for both the hydrodynamic and mooring-system responses using two representative quantities: the wave-elevation amplitude at a monitoring point on the weather side and the maximum tension in the primary load-bearing mooring line. The principal mesh parameters for the three resolution levels and the corresponding relative errors are summarized in Table 4.

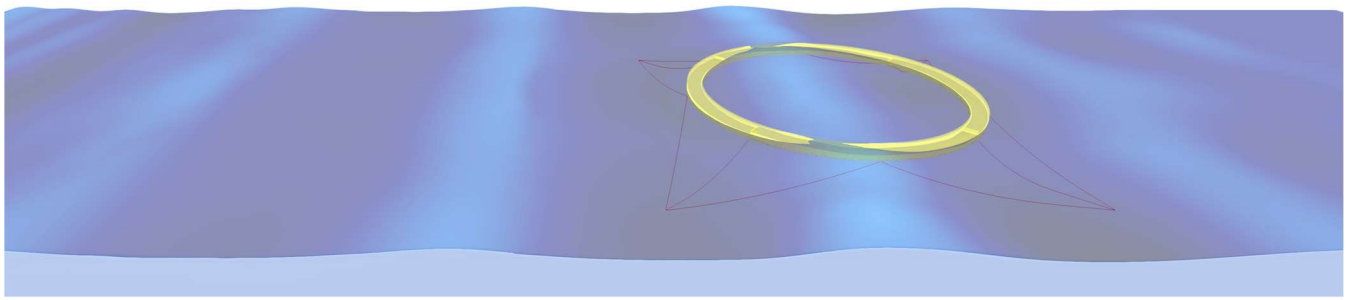
Table 4. Comparison of different mesh density schemes and their relative errors in computing wave elevation and maximum mooring tension.

Mesh Scheme	Core Mesh Size (m)	Number of Cells ($\times 10^4$)	Wave Elevation Amplitude (m)	Error of the Wave %	Max Mooring Tension (KN)	Error of Tension %
Coarse	0.06	79	0.0679	8.5	1.608	28.57
Medium	0.05	98	0.0728	1.9	2.217	5.8
Fine	0.04	118	0.0742	0	2.352	0

Based on the tabulated data and error analysis, both the hydrodynamic and mooring dynamic computational results gradually converge as the mesh density increases. Specifically, the relative errors in both wave amplitude and maximum mooring tension between the medium and fine meshes are strictly controlled within a minimal margin (6%). This indicates that when transitioning from the medium to the fine mesh, the variations in key fluid-structure interaction physical quantities are no longer sensitive, and the current computational accuracy fully satisfies the requirement for mesh independence. Weighing the high fidelity of the numerical simulation against the time costs of parallel computing, all subsequent fully coupled numerical simulations in this study are conducted using the medium-density mesh.

4.3. Overall Wave-Field Evolution and Analysis of Attenuation Mechanisms

The transient free-surface evolution shown in Figure 9 qualitatively illustrates the wave-transformation and attenuation processes during wave–breakwater interaction. As the incident wave crest reaches the weather-side outer wall, pronounced reflection and diffraction occur, redistributing the incident wave energy around the annular structure. After propagating over the weather-side section of the breakwater and entering the sheltered interior region, the free-surface amplitude decreases substantially, demonstrating the wave-attenuation effect of the single-ring breakwater.



(**a**)

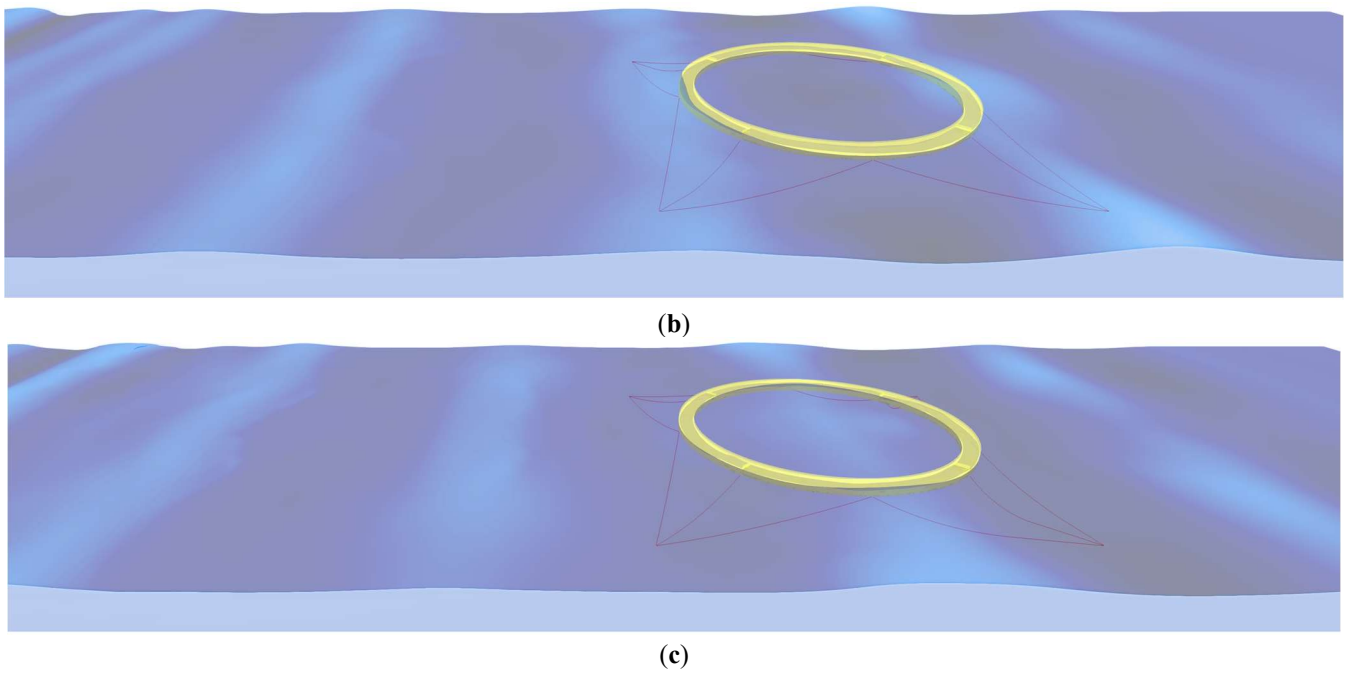


Figure 9. 3D snapshots of the transient free-surface evolution during the interaction between waves and the single-ring breakwater. (**a**) t = 60 s; (**b**) t = 61 s; (**c**) t = 62 s.

This study proposes that the wave attenuation performance of the breakwater arises primarily from two complementary mechanisms:

(1) Geometric scattering effect: When incident waves interact with the rigid outer wall of the annular structure, pronounced reflection and diffraction occur. These processes redistribute the incident wave energy and restrict its direct transmission into the sheltered region.

(2) Tuned-liquid-damper-like effect: The internal ballast water modifies the mass distribution, center of gravity, and moments of inertia of the structure. Under wave excitation, nonlinear sloshing within the compartments generates hydrodynamic forces that are out of phase with the wave-induced structural motion. This dynamic interaction suppresses the motion response of the breakwater, while viscous dissipation, turbulence, and local fluid impacts associated with sloshing contribute to energy loss, thereby further reducing wave transmission.

To provide a direct illustration of the wave attenuation performance of the water-ballasted single-ring breakwater, the wave-elevation time histories over 0–700 s at representative monitoring points on the weather side of the structure and within the central sheltered region are compared. Figure 10 presents the temporal variations in wave elevation under two representative extreme incident-wave conditions, with wave heights of 4 and 6 m. Under both conditions, the wave elevations transmitted into the sheltered region are substantially lower than those on the weather side. For the 6 m wave condition, the transmitted-wave signal exhibits more pronounced crest–trough asymmetry than that observed under the 4 m condition, consistent with the stronger nonlinear wave effects associated with the larger incident wave height. Nevertheless, its overall wave-elevation envelope remains markedly smaller than the corresponding weather-side response. These comparisons directly demonstrate the effective wave attenuation performance of the water-ballasted single-ring breakwater under the extreme deep-water wave conditions considered.

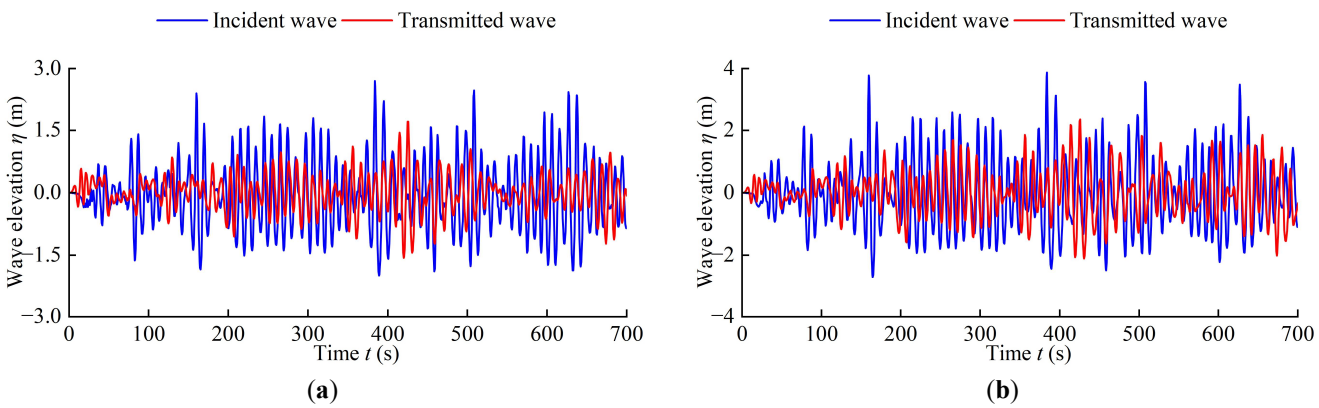


Figure 10. Comparison of transient time-history curves between the incident and transmitted waves of the water-ballasted single-ring breakwater. (**a**) Incident wave height of 4 m; (**b**) Incident wave height of 6 m.

5. Comparison of Compartmentalization Schemes of Ballasted Water

5.1. Configuration of Internal Compartmentalization Schemes

To systematically investigate the effects of internal compartmentalization on the hydrodynamic response and wave-dissipation mechanisms of the single-ring breakwater, four representative configurations are considered: an unballasted reference configuration (Empty) and three water-ballasted configurations comprising one, two, and four internal compartments, respectively, as shown in Figure 11a–d. The single-compartment configuration has an unpartitioned and fully interconnected interior, whereas the dual- and four-compartment configurations incorporate internal radial baffles to constrain ballast-water motion. The same initial ballast-water mass and filling level are prescribed for the three ballasted configurations to examine the effects of compartment number and baffle orientation on a consistent hydrostatic basis.

The incident-wave heading β is defined as the angle between the wave-propagation direction and the principal *x*-axis of the internal baffle layout. Two representative headings, $\beta = 0^{\circ}$ and 45°, are investigated. The 0° condition represents waves aligned with a principal baffle axis, whereas the 45° condition represents diagonal incidence relative to that axis. These headings were selected to represent two distinct wave–baffle interaction paths while taking advantage of the geometric symmetry of the annular structure. Because the Empty and 1C-B configurations are rotationally symmetric in plan, their responses are independent of heading, and the 0° results are used as their representative cases. Both headings are evaluated for the 2C-B and 4C-B configurations. Among the headings investigated, the 2C-B configuration achieves its lowest central-point transmission coefficient at 0°, whereas the 4C-B configuration achieves its lowest value at 45°. The following comparisons, therefore, use these selected best-performing headings; the term "best-performing" refers only to the two headings examined and should not be interpreted as a global optimum over all possible incident directions.

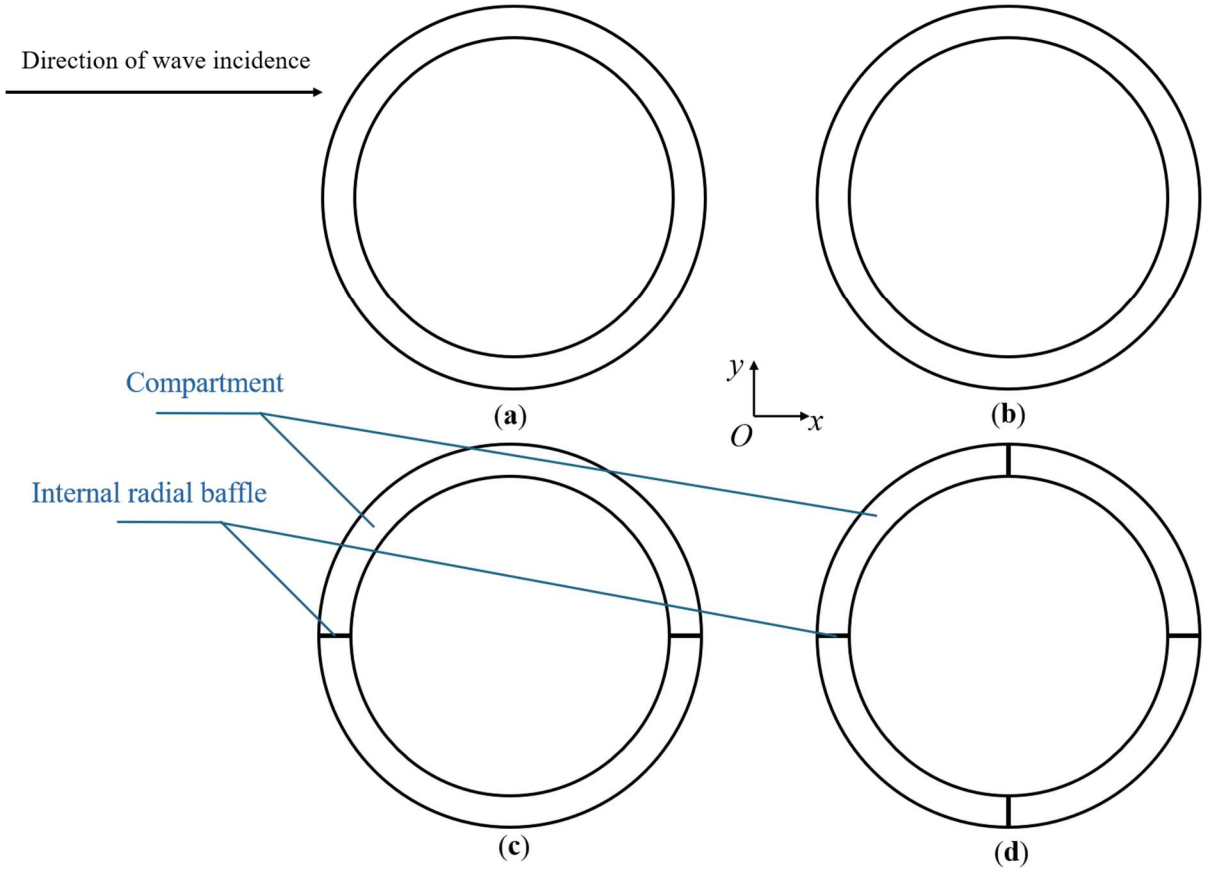


Figure 11. Geometric layouts of the four internal compartmentalization configurations. (**a**) Unballasted baseline; (**b**) Single-chamber ballasted; (**c**) Dual-chamber ballasted; (**d**) Quad-chamber ballasted.

5.2. Results and Discussion

5.2.1. Quantitative Evaluation of Transmission Coefficients

The wave transmission coefficient (K_t) is a core dimensionless metric for evaluating the sheltering performance of a breakwater [13,18,19], mathematically defined as the ratio of the significant wave height in the internal sheltered zone (H_t) to the external incident significant wave height (H_i):

$$K_t = \frac{H_t}{H_i} \tag{11}$$

where H_i is the incident significant wave height obtained from the weather-side monitoring point and H_t is the transmitted significant wave height obtained at the geometric center of the annular sheltered zone. Accordingly, K_t defined here is a local central-point transmission coefficient rather than a spatially averaged measure of the entire protected region. Because diffraction, wave interference, and internal sloshing can produce a spatially nonuniform wave field, the central-point value is used primarily for consistent comparison among the configurations. The free-surface snapshots and representative time histories provide complementary information on the broader wave-field evolution, but the quantitative K_t rankings reported below should be interpreted specifically with respect to the selected central monitoring location.

The quantitative wave-transmission results extracted from the free-surface-elevation records shown in Figure 12 are listed in Table 5. The table retains the incident significant wave height, transmitted significant wave height, and corresponding transmission coefficient, thereby allowing the wave-attenuation performance of each configuration to be evaluated precisely.

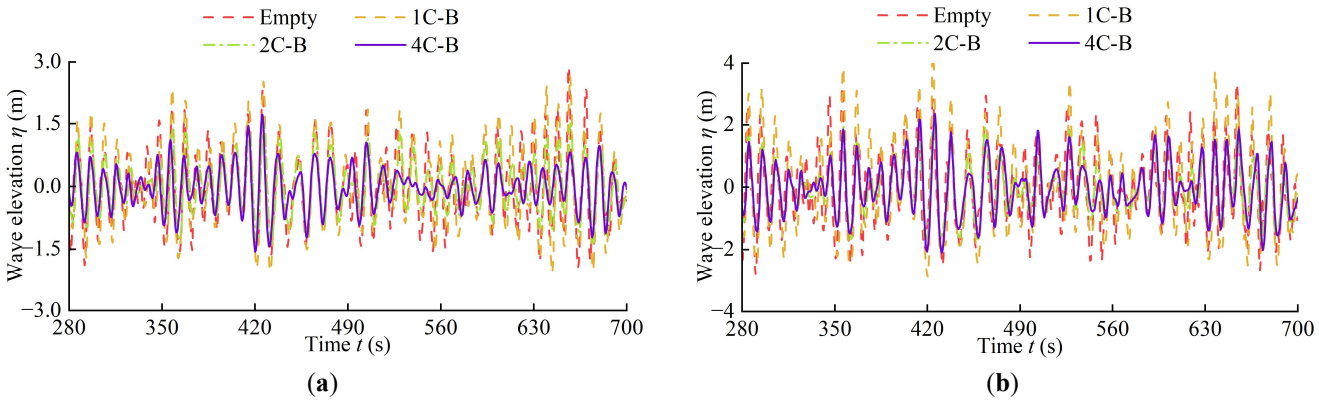


Figure 12. Comparison of transient time-history curves of wave elevation in the central sheltered zone for the four chamber configurations under their optimal wave headings. (**a**) Incident wave height of 4 m; (**b**) Incident wave height of 6 m.

Table 5. Comparison of transmission coefficients (K_t) among the four internal compartmentalization schemes under 4 m and 6 m incident wave heights.

Configuration	H_i = 4.0 m		H_i = 6.0 m	
	H_t (m)	K_t	H_t (m)	K_t
Empty	3.420	0.855	5.470	0.912
1C-B	3.395	0.849	5.180	0.863
2C-B	2.180	0.545	3.612	0.602
4C-B	1.805	0.451	2.955	0.493

For a more intuitive comparison of the relative attenuation performance, the (K_t) values reported in Table 5 are further presented as a bar chart in Figure 13. Table 5 provides the precise numerical results, whereas Figure 13 highlights the variation in (K_t) with internal compartmentalization and incident wave height.

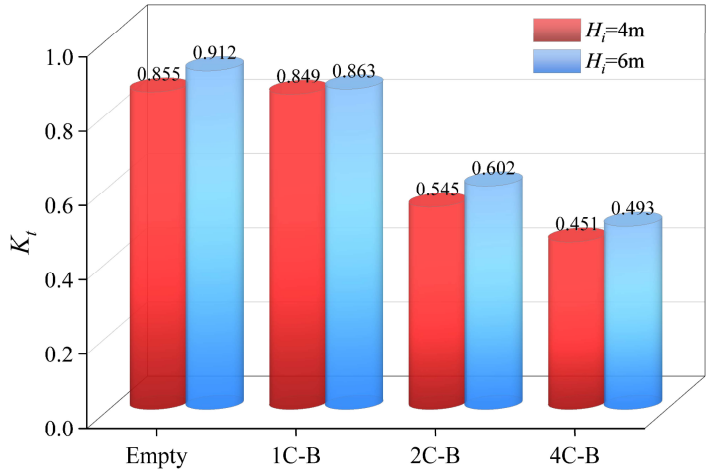


Figure 13. Comparison of wave transmission coefficients (K_t) among the four configurations under their respective optimal wave headings for (H_i = 4) and 6 m.

As shown in Table 5 and Figure 13, internal compartmentalization substantially improves wave attenuation, whereas the addition of ballast water without internal separation provides only limited benefit. At (H_i = 4) m, (K_t) decreases from 0.855 for the Empty configuration to 0.849, 0.545, and 0.451 for the 1C-B, 2C-B, and 4C-B configurations, respectively. Relative to the Empty configuration, the reductions in (K_t) are 0.7%, 36.3%, and 47.3%, respectively. The nearly identical (K_t) values of the Empty and 1C-B configurations indicate that the large, unpartitioned ballast-water mass does not effectively suppress wave transmission under this condition.

At (H_i = 6) m, the (K_t) values of the Empty, 1C-B, 2C-B, and 4C-B configurations are 0.912, 0.863, 0.602, and 0.493, respectively. Compared with the Empty configuration, 1C-B, 2C-B, and 4C-B reduce (K_t) by 5.4%, 34.0%, and 45.9%, respectively. Although the transmission coefficients increase with incident wave height, the 2C-B and 4C-B configurations continue to exhibit substantially lower (K_t) values than the Empty and 1C-B configurations.

The consistently superior performance of the compartmentalized configurations can be attributed to the restriction of large-scale internal sloshing by the baffles. The shortened internal flow paths and repeated interactions between the ballast water and baffles enhance local flow separation, vortex formation, and viscous energy dissipation. Increasing the number of compartments, therefore, strengthens wave attenuation, with the 4C-B configuration achieving the lowest transmission coefficient under both wave-height conditions.

5.2.2. Mooring-Tension Response

The survivability of the breakwater under extreme sea states depends strongly on the load-bearing performance of the mooring system. Given the symmetric arrangement of the mooring lines, the subsequent analysis focuses on the tension time histories of representative heavily loaded anchor chains located on the weather and lee sides. For completeness, additional mooring-tension results for the remaining anchor chains are provided in the Appendices A and B.

A comparison of Figures 14 and 15 show that appropriate internal compartmentalization not only improves wave attenuation performance but also reduces transient peaks in mooring tension. Under the extreme incident-wave condition with a wave height of 6 m, the large, unpartitioned ballast-water mass within the single-compartment configuration undergoes pronounced nonlinear sloshing and impact. The resulting internal fluid motion amplifies the motion response of the structure, thereby generating substantially higher transient tension peaks in the weather-side mooring lines.

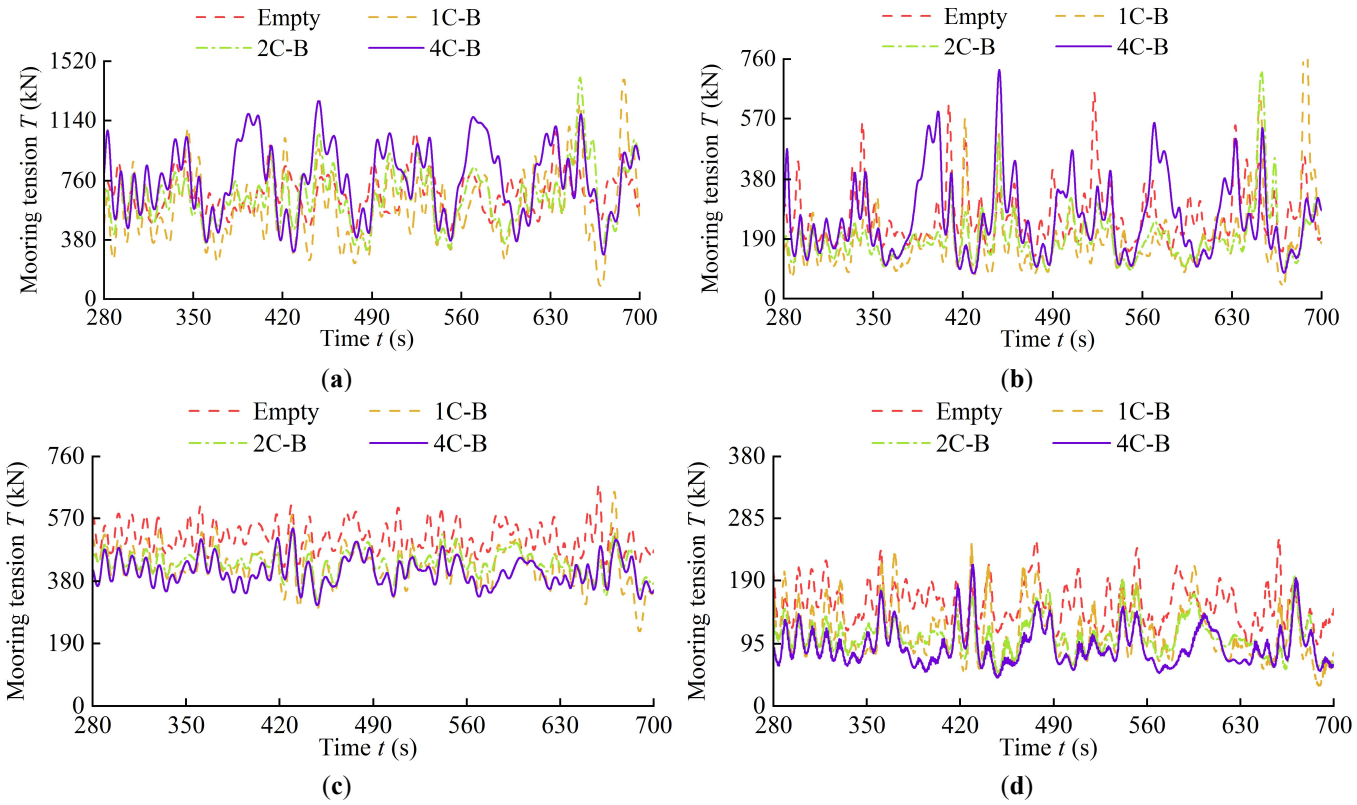


Figure 14. Impact of different compartmentalization schemes on the transient tension of key weather-side and lee-side mooring lines under a 4 m wave height. (**a**) Weather-side long mooring line; (**b**) Weather-side short mooring line; (**c**) Lee-side long mooring line; (**d**) Lee-side short mooring line.

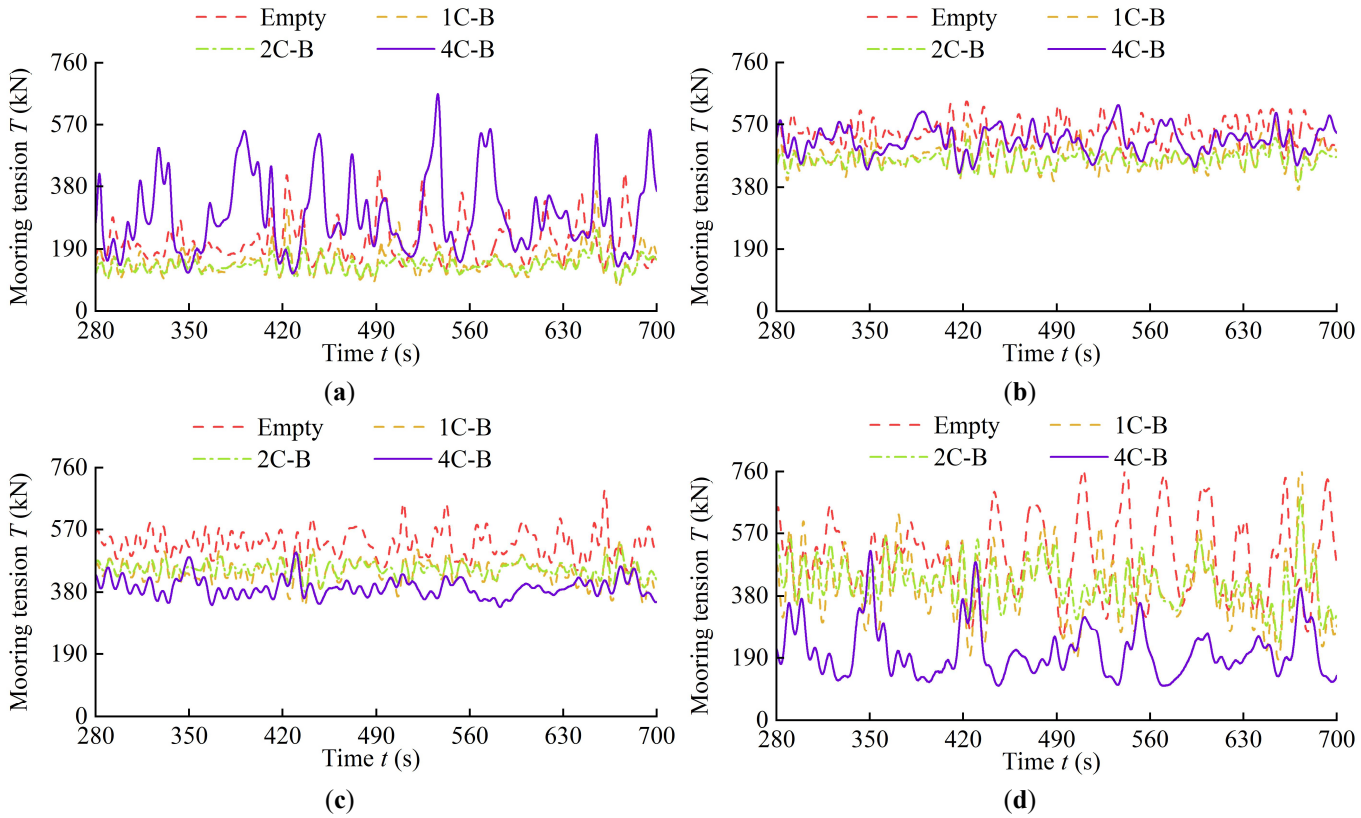


Figure 15. Impact of different compartmentalization schemes on the transient tension of key weather-side and lee-side mooring lines under a 6 m wave height. (**a**) Weather-side long mooring line; (**b**) Weather-side short mooring line; (**c**) Lee-side long mooring line; (**d**) Lee-side short mooring line.

A detailed comparison of the dual-compartment configuration under the 0° wave heading and the four-compartment configuration under the 45° wave heading reveals a clear hydrodynamic–engineering trade-off. Owing to its denser arrangement of diagonal internal baffles, the four-compartment configuration produces stronger blockage and fluid-impact effects on the weather side, leading to a modest increase in the tension of the primary weather-side mooring lines. However, its enhanced attenuation of transmitted wave energy results in lower mooring tensions on the lee side. By comparison, the dual-compartment configuration maintains effective wave attenuation while providing a more balanced hydrodynamic buffering effect, resulting in lower overall mooring loads on both the weather and lee sides. Therefore, when the overall mooring-load level, potential fatigue demand, and structural construction cost are considered together, the dual-compartment configuration under the 0° principal wave direction offers a more favorable balance and greater potential for practical engineering applications.

6. Conclusions

A fully coupled three-dimensional nonlinear fluid–structure interaction (FSI) numerical model based on the open-source platform OpenFOAM and incorporating the dynamic mooring solver MoorDyn was employed in this study and validated against physical experiments and published numerical results. The validated model was then used to investigate the wave attenuation performance and hydrodynamic responses of four internal compartment configurations under extreme irregular waves. The main conclusions are as follows:

(1) Ballast-water sloshing generates out-of-phase hydrodynamic forces and viscous dissipation, while internal baffles constrain large-scale sloshing; together, these effects suppress structural motion and mooring-tension peaks.

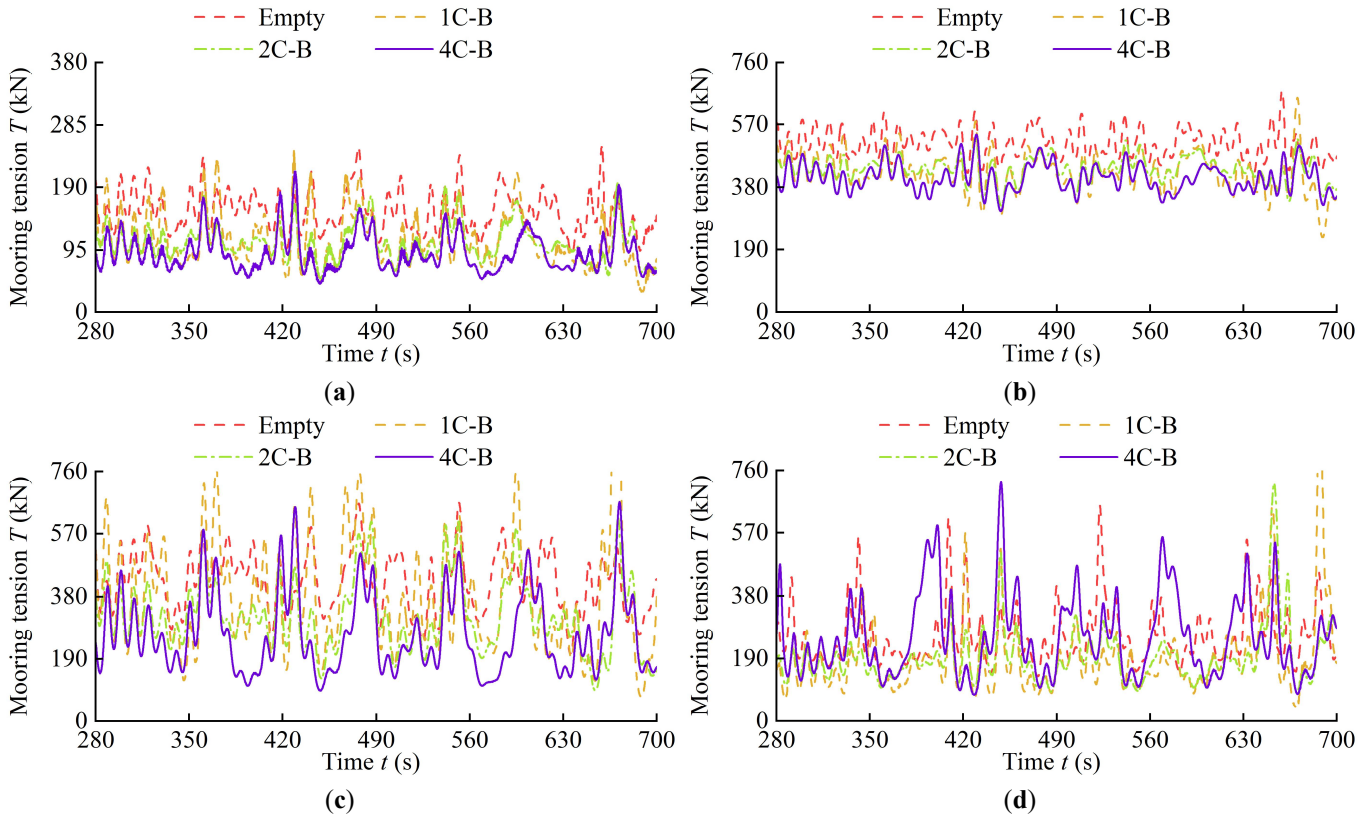
(2) At wave heights of 4 and 6 m, the four-compartment layout reduces (K_t) by 47.3% and 45.9%, respectively, relative to the unballasted case, whereas the single-compartment layout provides only limited improvement.

(3) The four-compartment layout achieves the strongest attenuation at 45° but increases weather-side tension. Considering mooring loads, fatigue, and cost, the dual-compartment layout at 0° provides the best overall balance.

Several limitations should be noted. The structure and baffles are treated as rigid, while mooring failure and nonlinear soil–anchor interaction are not considered. Moreover, the conclusions are limited to the investigated wave conditions, headings, and central monitoring point. Future work will incorporate hydroelasticity, broader environmental conditions, spatially averaged wave indicators, and mooring-fatigue assessment.

Appendix A. Transient Mooring Tensions Under a 4-m Incident-Wave Condition

This appendix presents the complete transient tension time-histories of the entire 12-line mooring array under the 4 m extreme incident wave height. Figure A1 compiles the dynamic tension fluctuations of Mooring Line 1 through Mooring Line 12 across the four internal compartmentalization schemes. This full spatial mapping reveals not only the substantial load reduction on the weather-side lines, but also the three-dimensional tension redistribution across the flank and lee-side mooring constraints.



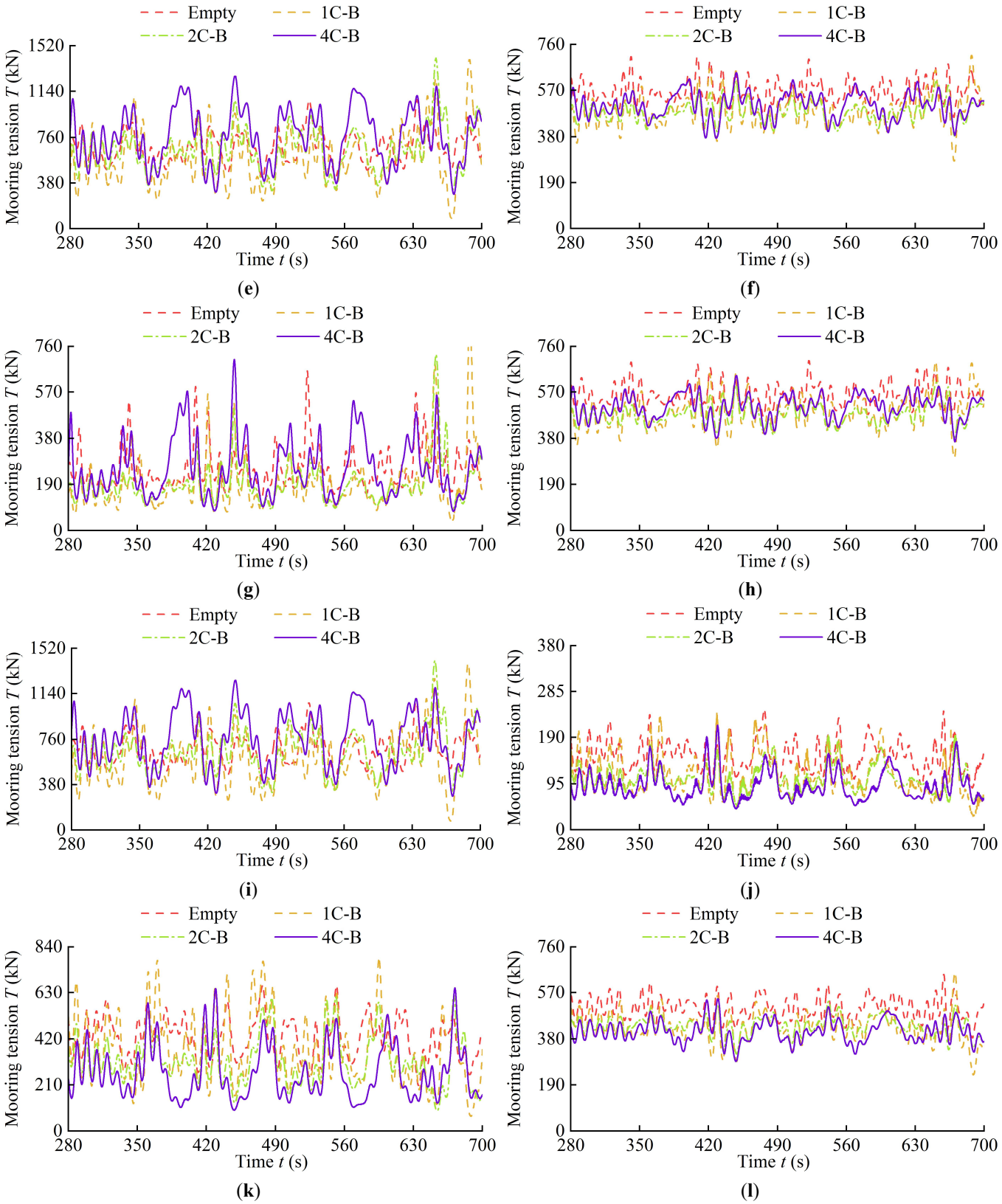
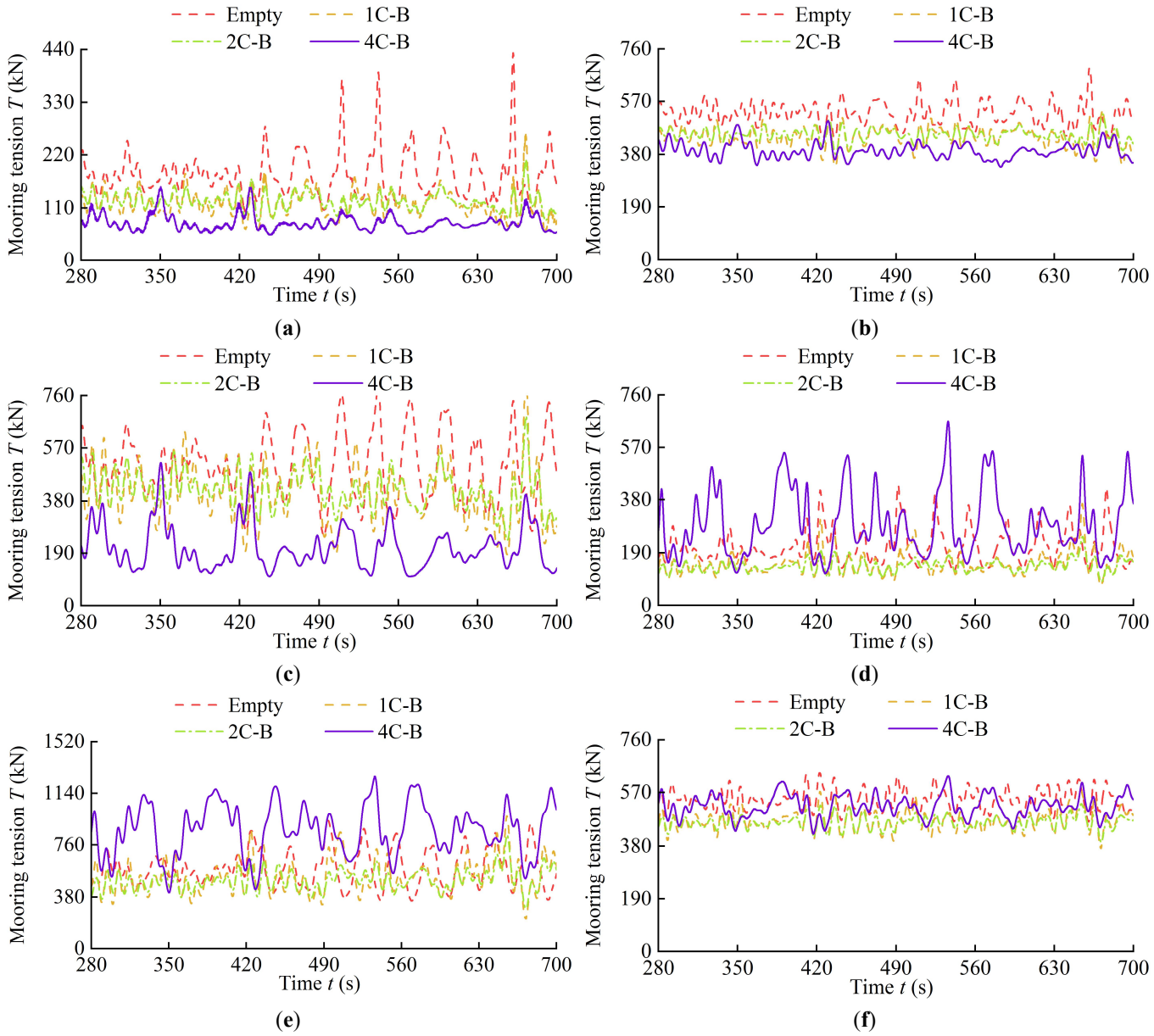


Figure A1. Transient tension time-histories of the 12 individual mooring lines under the 4 m incident wave height across different compartmentalization schemes. (**a**) Line 1; (**b**) Line 2; (**c**) Line 3; (**d**) Line 4; (**e**) Line 5; (**f**) Line 6; (**g**) Line 7; (**h**) Line 8; (**i**) Line 9; (**j**) Line 10; (**k**) Line 11; (**l**) Line 12.

Appendix B. Transient Mooring Tensions Under the 6 m Incident Wave Height

This appendix details the time-domain tension responses of the circumferentially distributed mooring lines under the severe 6 m extreme incident wave height. As depicted in Figure A2a–l, the intensified wave-structure interaction generally elevates the global tension baseline. However, tracking all 12 lines confirms that the internal Tuned Liquid Damper (TLD) effect robustly suppresses the extreme tension peaks of the weather-side lines without inducing secondary load spikes on the lee or flank lines, thereby demonstrating excellent omnidirectional mooring stability under survival sea states.



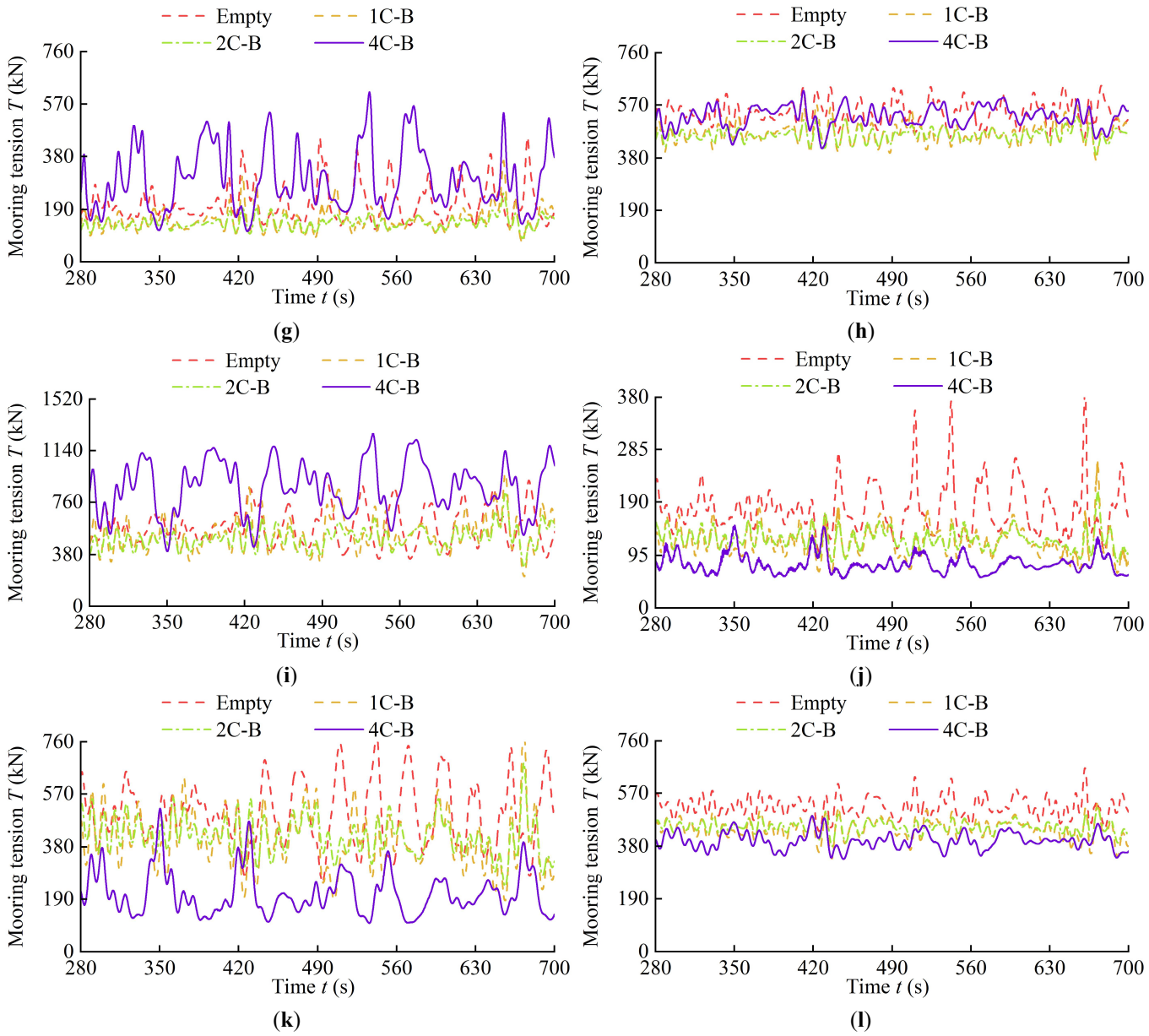


Figure A2. Transient tension time-histories of the 12 individual mooring lines under the 6 m incident wave height across different compartmentalization schemes. (**a**) Line 1; (**b**) Line 2; (**c**) Line 3; (**d**) Line 4; (**e**) Line 5; (**f**) Line 6; (**g**) Line 7; (**h**) Line 8; (**i**) Line 9; (**j**) Line 10; (**k**) Line 11; (**l**) Line 12.

Statement of the Use of Generative AI and AI-Assisted Technologies in the Writing Process

During the preparation of this manuscript, the authors used DeepSeek for English-language editing and to improve the clarity and readability of the manuscript. After using this tool, the authors reviewed and edited the content as needed and take full responsibility for the content of the published article.

Author Contributions

Conceptualization, J.L., X.Y. and Y.L.; Methodology, Y.L. and X.Y.; Software, Y.L., S.W. and J.W.; Validation, Y.L., S.W. and J.W.; Formal Analysis, Y.L.; Investigation, Y.L., S.W. and J.W.; Resources, J.L., X.Y. and Y.Y.; Data Curation, Y.L., S.W. and J.W.; Writing—Original Draft Preparation, Y.L.; Writing—Review and Editing, J.L., X.Y. and Y.Y.; Visualization, Y.L., S.W. and J.W.; Supervision, J.L., X.Y. and Y.Y.; Project Administration, X.Y. and Y.Y.; Funding Acquisition, J.L., X.Y. and Y.Y. All authors have read and agreed to the published version of the manuscript.

Ethics Statement

Not applicable.

Informed Consent Statement

Not applicable.

Data Availability Statement

Some corresponding numerical results of this study is available at https://www.scidb.cn/en/anonymous/TkJ6bXll (accessed on 2 September 2026). Other data that support the findings of this study are available upon reasonable request.

Funding

This research was funded by the National Key Research and Development Program of China, grant number 2022YFB4200701; the National Natural Science Foundation of China, grant number 52571308; and the Natural Science Foundation of Tianjin, grant number 24JCYBJC00870. The APC was waived by the publisher.

Declaration of Competing Interest

The authors declare that they have no known competing financial interests or personal relationships that could have appeared to influence the work reported in this paper.

References

1. Kjeldstad T, Lindholm D, Marstein E, Selj J. Cooling of floating photovoltaics and the importance of water temperature. *Sol. Energy* **2021**, *218*, 544–551. DOI:10.1016/j.solener.2021.03.022
2. Li Z, Chen D, Feng X. Hydroelastic and expansibility analysis of a modular floating photovoltaic system with multi-directional hinge connections. *Ocean Eng.* **2023**, *289*, 116218. DOI:10.1016/j.oceaneng.2023.116218
3. Cazzaniga R, Cicu M, Rosa-Clot M, Rosa-Clot P, Tina GM, Ventura C. Floating photovoltaic plants: Performance analysis and design solutions. *Renew. Sustain. Energy Rev.* **2018**, *81*, 1730–1741. DOI:10.1016/j.rser.2017.05.269
4. Garrod A, Neda Hussain S, Ghosh A, Nahata S, Wynne C, Paver S. An assessment of floating photovoltaic systems and energy storage methods: A comprehensive review. *Results Eng.* **2024**, *21*, 101940. DOI:10.1016/j.rineng.2024.101940
5. El Hammoumi A, Chalh A, Allouhi A, Motahhir S, El Ghzizal A, Derouich A. Design and construction of a test bench to investigate the potential of floating PV systems. *J. Clean. Prod.* **2021**, *278*, 123917. DOI:10.1016/j.jclepro.2020.123917
6. Majumder A, Kumar A, Innamorati R, Mastino CC, Cappellini G, Baccoli R, et al. Cooling Methods for Standard and Floating PV Panels. *Energies* **2023**, *16*, 7939. DOI:10.3390/en16247939
7. Kim SM, Oh M, Park HD. Analysis and Prioritization of the Floating Photovoltaic System Potential for Reservoirs in Korea. *Appl. Sci.* **2019**, *9*, 395. DOI:10.3390/app9030395
8. Oliveira-Pinto S, Stokkermans J. Marine floating solar plants: An overview of potential, challenges and feasibility. *Proc. Inst. Civ. Eng. Marit. Eng.* **2020**, *173*, 120–135. DOI:10.1680/jmaen.2020.10
9. Wang J, Lund PD. Review of Recent Offshore Photovoltaics Development. *Energies* **2022**, *15*, 7462. DOI:10.3390/en15207462
10. Fan Y, Li J, Liu S, Zhang H. A study of wave forces on a vertical truncated cylinder with different submergence depths. *Ocean Eng.* **2024**, *313*, 119489. DOI:10.1016/j.oceaneng.2024.119489
11. Zhai G, Zhou T, Ma Z, Ren N, Chen J, Teh HM. Comparison of impulsive wave forces on a semi-submerged platform deck, with and without columns and considering air compressibility effects, under regular wave actions. *Eng. Appl. Comput. Fluid Mech.* **2021**, *15*, 1932–1953. DOI:10.1080/19942060.2021.1999858
12. Zhang N, Xiao L, Zou Q, Cummins C. Large-scale wave basin experimental study on the spatio-temporal distribution of wave impact loads on a semi-submersible platform. *Ocean Eng.* **2025**, *327*, 120991. DOI:10.1016/j.oceaneng.2025.120991
13. Dai J, Wang CM, Utsunomiya T, Duan W. Review of recent research and developments on floating breakwaters. *Ocean Eng.* **2018**, *158*, 132–151. DOI:10.1016/j.oceaneng.2018.03.083

14. Fouladi MQ, Bahmanpouri F, Rezazadeh S, Kollolemad F, Mashayekhi M, Viccione G. Investigating the sidewall's effects on π-shaped floating breakwaters interacting with water waves by the scaled boundary FEM. *Ocean Eng.* **2023**, *284*, 115200. DOI:10.1016/j.oceaneng.2023.115200
15. Ji CY, Chen X, Cui J, Gaidai O, Incecik A. Experimental study on configuration optimization of floating breakwaters. *Ocean Eng.* **2016**, *117*, 302–310. DOI:10.1016/j.oceaneng.2016.03.002
16. Bayram A. Experimental study of a sloping float breakwater. *Ocean Eng.* **2000**, *27*, 445–453. DOI:10.1016/S0029-8018(98)00080-8
17. Williams AN, Lee HS, Huang Z. Floating pontoon breakwaters. *Ocean Eng.* **2000**, *27*, 221–240. DOI:10.1016/S0029-8018(98)00056-0
18. Yin Z, Ni Z, Luan Y, Zhang X, Li J, Li Y. Hydrodynamic characteristics of a box-type floating breakwater with restrained piles under regular waves. *Ocean Eng.* **2023**, *280*, 114408. DOI:10.1016/j.oceaneng.2023.114408
19. Ning DZ, Zhao XL, Zhao M, Hann M, Kang HG. Analytical investigation of hydrodynamic performance of a dual pontoon WEC-type breakwater. *Appl. Ocean Res.* **2017**, *65*, 102–111. DOI:10.1016/j.apor.2017.03.012
20. Christensen ED, Bingham HB, Skou Friis AP, Larsen AK, Jensen KL. An experimental and numerical study of floating breakwaters. *Coast. Eng.* **2018**, *137*, 43–58. DOI:10.1016/j.coastaleng.2018.03.002
21. Liu Z, Wang Y, Wang W, Hua X. Numerical modeling and optimization of a winged box-type floating breakwater by Smoothed Particle Hydrodynamics. *Ocean Eng.* **2019**, *188*, 106246. DOI:10.1016/j.oceaneng.2019.106246
22. Cho IH. Transmission coefficients of a floating rectangular breakwater with porous side plates. *Int. J. Nav. Archit. Ocean Eng.* **2016**, *8*, 53–65. DOI:10.1016/j.ijnaoe.2015.10.002
23. Dou P, Xue MA, Zheng J, Zhang C, Qian L. Numerical and experimental study of tuned liquid damper effects on suppressing nonlinear vibration of elastic supporting structural platform. *Nonlinear Dyn* **2020**, *99*, 2675–2691. DOI:10.1007/s11071-019-05447-y
24. Xue MA, Dou P, Zheng J, Lin P, Yuan X. Pitch motion reduction of semisubmersible floating offshore wind turbine substructure using a tuned liquid multicolumn damper. *Mar. Struct.* **2022**, *84*, 103237. DOI:10.1016/j.marstruc.2022.103237
25. Yang Z, Ji X, Xie M, Li J, Zhang H, Wang D. Experimental study on the dynamic response of a water ballast type floating breakwater. *Ocean Eng.* **2021**, *233*, 109012. DOI:10.1016/j.oceaneng.2021.109012
26. Sun B, Zhang H, Yang S, Li C. Experimental investigation on the wave-attenuating performance and shape optimization of water ballast type floating breakwater. *Ocean Eng.* **2022**, *248*, 110848. DOI:10.1016/j.oceaneng.2022.110848
27. Xue MA, He Y, Yuan X, Cao Z, Odoom JK. Numerical and experimental study on sloshing damping effects of the porous baffle. *Ocean Eng.* **2023**, *285*, 115363. DOI:10.1016/j.oceaneng.2023.115363
28. Zhao X, Du X, Li M, Göteman M. Semi-analytical study on the hydrodynamic performance of an interconnected floating breakwater-WEC system in presence of the seawall. *Appl. Ocean Res.* **2021**, *109*, 102555. DOI:10.1016/j.apor.2021.102555
29. Masoudi E, Marshall A. Diffraction of waves by multi-pontoon rectangular floating breakwaters. *Ocean Eng.* **2024**, *310*, 118789. DOI:10.1016/j.oceaneng.2024.118789
30. Gao J, Mi C, Song Z, Liu Y. Transient gap resonance between two closely-spaced boxes triggered by nonlinear focused wave groups. *Ocean Eng.* **2024**, *305*, 117938. DOI:10.1016/j.oceaneng.2024.117938
31. Hu KZ, Xu TJ, Wang S. Hydrodynamic investigation of a new type of floating breakwaters integrated with porous baffles. *Appl. Ocean Res.* **2025**, *154*, 104380. DOI:10.1016/j.apor.2024.104380
32. Dunbar AJ, Craven BA, Paterson EG. Development and validation of a tightly coupled CFD/6-DOF solver for simulating floating offshore wind turbine platforms. *Ocean Eng.* **2015**, *110*, 98–105. DOI:10.1016/j.oceaneng.2015.08.066
33. Palm J, Eskilsson C, Paredes GM, Bergdahl L. Coupled mooring analysis for floating wave energy converters using CFD: Formulation and validation. *Int. J. Mar. Energy* **2016**, *16*, 83–99. DOI:10.1016/j.ijome.2016.05.003
34. Eskilsson C, Palm J. High-fidelity modelling of moored marine structures: Multi-component simulations and fluid-mooring coupling. *J. Ocean Eng. Mar. Energy* **2022**, *8*, 513–526. DOI:10.1007/s40722-022-00263-w
35. Domínguez JM, Crespo AJC, Hall M, Altomare C, Wu M, Stratigaki V, et al. SPH simulation of floating structures with moorings. *Coast. Eng.* **2019**, *153*, 103560. DOI:10.1016/j.coastaleng.2019.103560
36. Yang X, Jiang L, Yao Y, Gao X, Yan X, Shao N, et al. Energy Harness and Wake Structure of "Cir-Tri-Att" Oscillators for Flow-Induced Motion Tidal Energy Conversion System. *Mar. Energy Res.* **2025**, *2*, 10002. DOI:10.70322/mer.2025.10002
37. Lian J, Yang S, Yan L, Yang X, Yao Y, Liang C. Binocular Camera-Based Depth Recognition for Motion Monitoring and Response Analysis of Flexible Floating Structures for Offshore Photovoltaics. *Mar. Energy Res.* **2025**, *2*, 10019. DOI:10.70322/mer.2025.10019

38. Li X, Xiao Q, Zhou Y, Ning D, Incecik A, Nicoll R, et al. Coupled CFD-MBD numerical modeling of a mechanically coupled WEC array. *Ocean Eng.* **2022**, *256*, 111541. DOI:10.1016/j.oceaneng.2022.111541
39. Wei Y, Yu S, Jin P, Huang L, Elsherbiny K, Tezdogan T. Coupled analysis between catenary mooring and VLFS with structural hydroelasticity in waves. *Mar. Struct.* **2024**, *93*, 103516. DOI:10.1016/j.marstruc.2023.103516
40. Chen H, Medina TA, Cercos-Pita JL. CFD simulation of multiple moored floating structures using OpenFOAM: An open-access mooring restraints library. *Ocean Eng.* **2024**, *303*, 117697. DOI:10.1016/j.oceaneng.2024.117697
41. Hall M, Goupee A. Validation of a lumped-mass mooring line model with DeepCwind semisubmersible model test data. *Ocean Eng.* **2015**, *104*, 590–603. DOI:10.1016/j.oceaneng.2015.05.035
42. Lee SC, Song S, Park S. Platform Motions and Mooring System Coupled Solver for a Moored Floating Platform in a Wave. *Processes* **2021**, *9*, 1393. DOI:10.3390/pr9081393
43. Chen H, Hall M. CFD simulation of floating body motion with mooring dynamics: Coupling MoorDyn with OpenFOAM. *Appl. Ocean Res.* **2022**, *124*, 103210. DOI:10.1016/j.apor.2022.103210
44. Jeon W, Park S, Cho S. Moored motion prediction of a semi-submersible offshore platform in waves using an OpenFOAM and MoorDyn coupled solver. *Int. J. Nav. Archit. Ocean Eng.* **2023**, *15*, 100544. DOI:10.1016/j.ijnaoe.2023.100544
45. Yuan X, Cao Z, Xue MA, Li L, Zheng J. Experimental study on effects of floating breakwater filled with ballast water on wave attenuation. *Ocean Eng.* **2025**, *341*, 122720. DOI:10.1016/j.oceaneng.2025.122720
46. Jacobsen NG, Fuhrman DR, Fredsøe J. A Wave Generation Toolbox for the Open-Source CFD Library: OpenFOAM. *Int. J. Numer. Methods Fluids* **2012**, *70*, 1073–1088. DOI:10.1002/fld.2726
47. Hirt CW, Nichols BD. Volume of Fluid (VOF) Method for the Dynamics of Free Boundaries. *J. Comput. Phys.* **1981**, *39*, 201–225. DOI:10.1016/0021-9991(81)90145-5
48. Mohapatra SC, da Silva Bispo IB, Guo Y, Guedes Soares C. Analysis of Wave-Induced Forces on a Floating Rectangular Box with Analytical and Numerical Approaches. *J. Marine. Sci. Appl.* **2024**, *23*, 113–126. DOI:10.1007/s11804-024-00385-7
49. Lian J, Yan L, Yang S, Yao Y, Yang X, Liang C. Numerical and experimental analysis of wave-slamming characteristics of offshore floating photovoltaic structures. *Ocean Eng.* **2026**, *356*, 125242. DOI:10.1016/j.oceaneng.2026.125242